CHALMERS
UNIVERSITY OF TECHNOLOGY

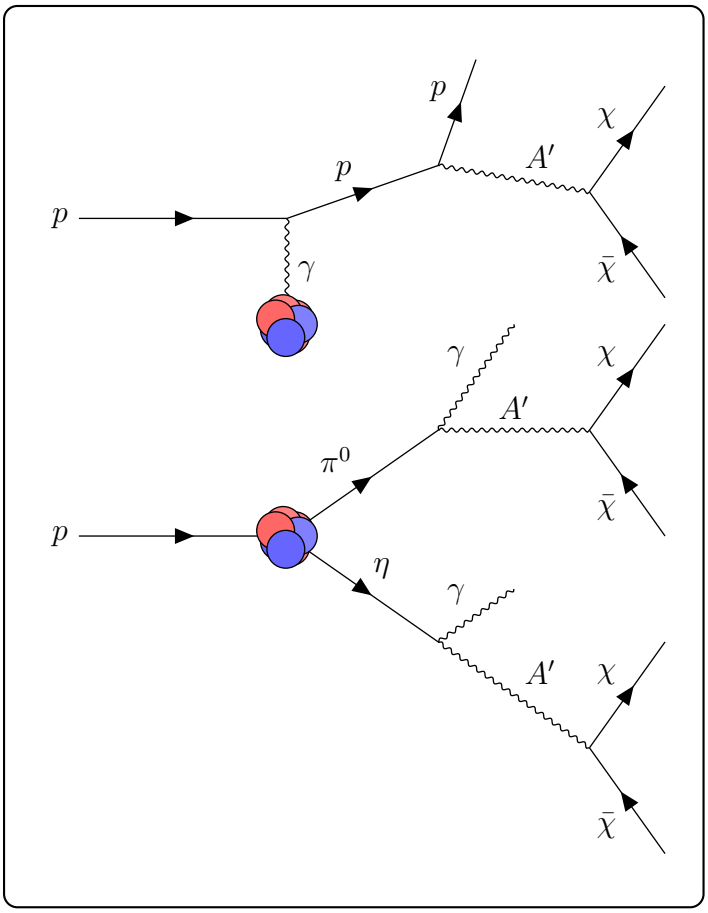

Simulating Light Dark Matter Signals at SHiP

Master's thesis in Physics

ELIAS SVENSSON

DEPARTMENT OF PHYSICS
CHALMERS UNIVERSITY OF TECHNOLOGY
Gothenburg, Sweden 2025
www.chalmers.se

Master's thesis 2025

Simulating Light Dark Matter Signals at SHiP

ELIAS SVENSSON

CHALMERS
UNIVERSITY OF TECHNOLOGY

Department of Physics
Division of Subatomic, High-Energy and Plasma Physics
Theoretical Subatomic Physics
Chalmers University of Technology
Gothenburg, Sweden 2025

Simulating Light Dark Matter Signals at SHiP
Elias Svensson

Supervisor: Riccardo Catena & Taylor Gray, Department of Physics
Examiner: Riccardo Catena, Department of Physics

Master's Thesis 2025
Department of Physics
Division of Subatomic, High-Energy and Plasma Physics
Theoretical Subatomic Physics
Chalmers University of Technology
SE-412 96 Gothenburg
Telephone +46 31 772 1000

Cover: Schematic illustration of proton-nucleus interactions resulting in the production of mesons, photons, and dark photons. The dark photons subsequently decay into dark matter particles. The diagram illustrates the three interaction channels considered for dark sector particle production in this thesis – π^0 decay, η decay, and proton bremsstrahlung – as discussed in Section 2.4.

Typeset in LaTeX
Printed by Chalmers Reproservice
Gothenburg, Sweden 2025

Simulating Light Dark Matter Signals at SHiP
Elias Svensson
Department of Physics
Chalmers University of Technology

Abstract

Dark matter remains one of the most compelling mysteries in modern physics, with a wide range of astrophysical and cosmological observations providing strong evidence for its existence. Among the many proposed candidates, light dark matter, with masses below the GeV scale, has gained increasing interest, partly due to its accessibility in current and next-generation accelerator-based experiments. An interesting framework for light dark matter involves a massive dark photon mediator A', which kinetically mixes with the Standard Model photon, enabling interactions between the visible and dark sectors.

This thesis focuses on the sensitivity of the SHiP (Search for Hidden Particles) experiment – a planned proton beam-dump experiment at the CERN Super-Proton-Synchrotron (SPS) – to light dark matter scenarios. This experiment is designed to probe feebly interacting particles and is expected to significantly extend the parameter space coverage for light dark sector particles. The analysis adopts a benchmark model characterized by a minimal dark sector with a complex scalar dark matter candidate χ, a dark coupling $\alpha_D = 0.1$, and a mediator mass set to $m_{A'} = 3m_\chi$.

Simulations are performed using two independent tools: **BdNMC**, a standalone dark matter Monte Carlo generator, and **MadDump**, a plugin for the **MadGraph5_aMC@NLO** framework tailored for beam dump and fixed-target experiments. A comparative analysis of these tools is conducted in the context of the complex scalar model, highlighting methodological differences and their impact on predicted signal rates. Furthermore, the sensitivity studies for the SHiP experiment are extended to fermionic dark matter scenarios, including both Dirac and Majorana candidates, resulting in updated exclusion contours and emphasizing the experiment's discovery potential across these different dark matter hypotheses.

Keywords: Light Dark Matter (LDM), Dark Photon, Beam Dump Experiments, SHiP, Hidden Sector, Dark Sector, BdNMC, MadDump, Dark Matter Simulations, Beyond Standard Model (BSM)

Acknowledgements

I would like to express my deepest gratitude to my examiner and supervisor, Riccardo Catena, for guiding me through my thesis despite an extremely busy schedule. Your feedback and words of encouragement have been incredibly helpful and truly motivating.

I am also profoundly thankful to my other supervisor, Taylor Gray, for always keeping their door open and generously sharing their knowledge, enthusiasm, and support. Your patience and willingness to help me through the many challenges and questions I brought to you have been invaluable.

To my friends – both those who have been with me throughout these five years at Chalmers and those who joined more recently – thank you for making this time so enjoyable and memorable.

Lastly, I want to express my heartfelt thanks to my family for their unwavering support, curiosity, and love. Your encouragement – and the much-needed moments of distraction – made this journey possible.

Elias Svensson, Gothenburg, June 2025

List of Acronyms

Below is the list of acronyms that have been used throughout this thesis listed in alphabetical order:

BAO	Baryon Acoustic Oscillations
BBN	Big Bang Nucleosynthesis
CMB	Cosmic Microwave Background
CS	Complex Scalar
DF	Dirac Fermion
DM	Dark Matter
HSD	Hidden Sector Detector
IGM	Intergalactic Medium
LDM	Light Dark Matter
LDMX	Light Dark Matter eXperiment
MF	Majorana Fermion
MOND	Modified Newtonian Dynamics
POT	Protons On Target
SHiP	Search for Hidden Particles
SLAC	Stanford Linear Accelerator Center
SM	Standard Model
SND	Scattering Neutrino Detector
SPS	Super-proton-Synchrotron
TeVeS	Tensor-Vector-Scalar
UFO	Universal FeynRules Output

Contents

List of Figures

List of Tables

1

Introduction

For centuries, humanity's understanding of the universe has been shaped by what we can see – glowing stars, luminous galaxies, and vast nebulae scattered across the cosmic expanse. Yet, as our ability to observe the skies has advanced, so too has a growing realization: much of the universe is hidden from view. A vast, unseen mass pervades space, influencing the motion of stars and galaxies in ways that cannot be explained by visible matter alone. This enigmatic substance – what we now call dark matter – remains one of the greatest mysteries in modern physics and cosmology.

The idea that celestial bodies could be detected not by their light, but by their gravitational influence, predates even the concept of dark matter itself. In the early 19th century, German astronomer Friedrich Bessel, analyzing deviations in the motions of Sirius and Procyon, argued that unseen celestial bodies must be exerting a gravitational pull on these stars. He famously stated, "But light is no real property of mass. The existence of numberless visible stars can prove nothing against the evidence of numberless invisible ones" [1].

Later that same century, Lord Kelvin argued that the observed velocities of certain stars could not be explained by the gravitational influence of visible stars alone. He proposed that additional mass must be present in the form of unseen "dark bodies". He wrote, "Many of our supposed thousand million stars, perhaps a great majority of them, may be dark bodies". Although he did not think of this as exotic new particles, his suggestion of unseen matter is today a foundational concept in astrophysics [2].

In 1933, Fritz Zwicky attempted to estimate the mass of the Coma Cluster by analyzing the velocity dispersion of its member galaxies. Using the virial theorem, his calculations suggested that the total mass of the cluster was approximately 400 times greater than the mass of its luminous matter. This discrepancy he assigned to "dunkle Materie" or "dark matter", stating, "If this should be verified, it would lead to the surprising result that dark matter exists in much greater density than luminous matter" [3].

For comparison, modern observations indicate that dark matter constitutes roughly 84% of all matter in the universe. However, matter itself comprises only about 32% of the universe's total mass-energy content, with the remainder attributed to "dark energy" (yet another profound mystery in modern physics) [4].

Since the times of Bessel, Lord Kelvin, Zwicky, and other pioneering researchers, evidence for dark matter has continued to accumulate. Some of the most compelling support comes from observations of colliding galaxy clusters – such as the Bullet Cluster – and the Cosmic Microwave Background [5]. These phenomena, along with others, will be explored in greater detail in the coming sections.

Still today, the mass range of viable dark matter candidates spans many orders of magnitude. This broad range can be constrained by theoretical considerations – for instance, by assuming that dark matter was thermally produced in the early universe through the so-called freeze-out mechanism. Within this framework, its heavier candidates have been the primary focus of experimental searches over the past few decades. However, the lack of any conclusive signal has gradually brought attention to the lighter end of the spectrum – the domain of light dark matter [6].

The experiment central to this thesis – Search for Hidden Particles (SHiP) – is being developed to probe this light dark matter class of candidates with high sensitivity. To assess SHiP's discovery potential and guide its design, detailed simulations play a critical role. Understanding the simulation tools – their capabilities, assumptions, and limitations – is therefore essential.

Thesis Aim and Structure

This thesis aims to identify the key differences between two simulation tools – **BdNMC** and **MadDump** – for estimating sensitivity to light dark matter scenarios in the context of the SHiP experiment. A further objective is to validate the performance of both tools and asses their reliability. Additionally, the study seeks to extend the exclusion limits of the SHiP experiment through the inclusion of two light dark matter models not previously studied in this context: the Majorana and Dirac fermion candidates. This includes validating **MadDump** as a simulation tool capable of handling general dark matter model inputs.

The thesis is structured as follows:

Section 2.1 begins by outlining some of the most prominent evidence for the existence of dark matter, followed by a discussion of its possible origins in the early universe. Section 2.3.1 then reviews some cosmological constraints on the properties of various dark matter scenarios.

Section 2.3.2 introduces the light dark matter models studied throughout this work. Detection strategies and relevant experiments are subsequently discussed, culminating in a detailed description of the SHiP experiment in Section 2.4, along with the dark matter production and detection mechanisms relevant to this thesis.

Section 3.1 presents the methodology behind the two simulation tools, and Section 3.2 outlines the workflow developed for their use in this study.

The results and key findings are presented in Section 4, followed by a discussion and analysis in Section 5.

Finally, the thesis concludes with Section 6, which summarizes the main outcomes and offers an outlook on future directions for research in this area.

2

Background

The Standard Model of particle physics stands as one of the most successful and experimentally validated theories in physics. It provides a comprehensive framework for understanding the fundamental particles and their interactions – excluding gravity – and has accurately predicted a wide range of phenomena, from the existence of the Higgs boson to the behavior of subatomic particles in high-energy collisions. Despite its success, the Standard Model is not a complete theory of nature. It does not incorporate gravity, and it fails to account for several key cosmological observations, such as the accelerated expansion of the universe and the presence of dark matter. These shortcomings strongly suggest the need for physics beyond the Standard Model – an extended framework that could potentially reveal the nature of dark matter and deepen our understanding of the universe.

2.1 The Case for Dark Matter

As the name suggests, dark matter (DM) is "dark" because it interacts very weakly – if at all – electromagnetically, making direct detection challenging. This gives some insight into why all current evidence for the existence of DM is based on the gravitational effects it exhibits.

One of the most significant observable effects is gravitational lensing – a phenomenon predicted by Einstein's theory of general relativity [7], though the term itself was not coined by him. In essence, gravitational lensing refers to the bending of light rays as they travel through space-time distorted by a gravitational field. Four years after analyzing the Coma Cluster, Zwicky proposed that this effect could serve as a powerful tool for accurately determining the masses of nebulae [8]. Given DM's gravitational influence, gravitational lensing has similarly become an essential method for detecting and studying its distribution in the universe [9].

Another piece of evidence for DM comes from galaxy rotation curves. According to Newtonian mechanics and the distribution of visible matter in galaxies, the rotational velocity $v(r)$ of stars and gas at a distance r from the galactic center should decrease with distance, following $v(r) \propto r^{-1/2}$. This decline ensures that the gravitational pull from the enclosed mass is sufficient to maintain orbital motion. However, observations tell a different story: beyond the central bulge, the rotation curves tend to flatten, with velocities remaining roughly constant at large radii, see figure 2.1. This unexpected behavior hints at the contribution from an additional, unseen mass

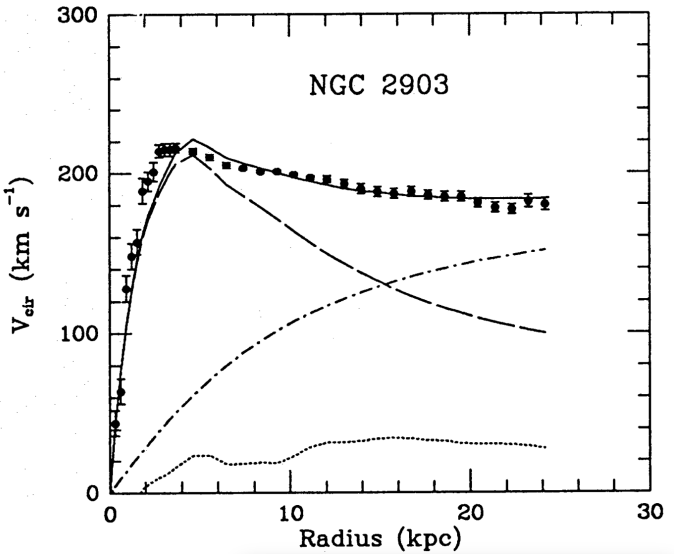

Figure 2.1: Rotation curve of the galaxy NGC 2903, showing a fit that includes a dark matter halo (solid line). The contributions from the stellar disk, gas, and the dark halo are represented by the dashed, dotted, and dash-dot lines, respectively. The observed flattening of the rotation curve at large radii is well explained by the presence of a dark matter halo. Figure credit: [11]

component that extends well beyond the visible structure of the galaxy – a DM halo [10].

One of the most striking observations supporting the existence of DM is the Bullet Cluster (1E 0657-558). The Bullet Cluster consists of two galaxy clusters that have collided and passed through each other. During such a collision, the stars within the galaxies behave like nearly collisionless particles, continuing along their trajectories with minimal direct interaction, aside from gravitational effects. In contrast, the hot plasma components experience significant ram pressure, causing them to slow down and thus separate from the galaxies. In a universe without DM, one would expect the majority of the mass to follow the distribution of the X-ray-emitting plasma. However, if DM is the dominant mass component, the bulk of the mass should instead align with the galaxies, as DM – due to its weakly interacting nature – would similarly pass through the collision. Observations of the Bullet Cluster strongly support the latter scenario [12]. As shown in Figure 2.2, gravitational lensing measurements reveal that the majority of the mass (blue) is distinctly separated from the X-ray-emitting plasma (pink), providing compelling evidence for the presence of DM.

Additional evidence for DM comes from the observed anisotropies in the cosmic microwave background (CMB). In the early universe, ordinary (baryonic) matter was subject to both gravitational attraction and opposing pressure forces from photons. As gravity compresses the hot photon-baryon plasma in denser regions, the photon pressure eventually starts to dominate, and rarefaction occurs. This cyclical process produces oscillations in the plasma known as baryon acoustic oscillations (BAO) [14].

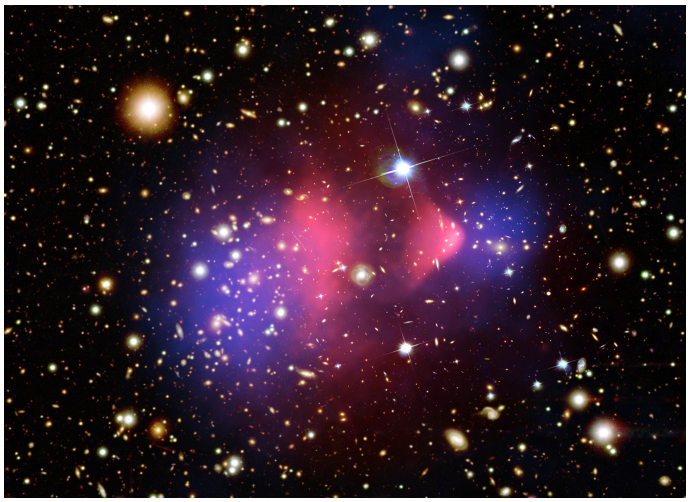

Figure 2.2: Composite image of the Bullet Cluster (1E 0657-558). The orange and white dots in the background show galaxies, from optical images from the Magellan and the Hubble Space Telescope. The hot intracluster gas (pink), captured by an X-ray image from the Chandra telescope, is separate from the bulk of the cluster's mass (blue), as measured through gravitational lensing, indicating that nearly all matter in the clusters is dark. Figure credit: [13]

DM, in contrast, interacts primarily through gravity and is pressureless. If the DM was cold (non-relativistic), it would have allowed spatial density fluctuations to persist, unlike hot (relativistic) DM, which would rapidly erase such fluctuations. These granules of higher DM density would grow due to the slightly higher gravitational attraction, and act as gravitational potential wells for the photon-baryon plasma [14]. The presence of cold DM in these early stages of the universe would therefore influence the oscillations and leave an imprint on the CMB temperature power spectrum, which serves as a snapshot of the universe at the time of photon decoupling. Each peak in the spectrum, seen in Figure 2.3, carries information about different cosmological parameters – for instance, the first peak supports the conclusion that the universe is spatially flat. Most notably in the setting of this thesis, the prominence of the third peak of this spectrum provides strong evidence that DM was present and played a crucial role in shaping the universe's evolution [15].

Not everyone is comfortable with the invocation of a new, unseen type of matter. Instead, some have proposed modifications to the laws of gravity in lieu, dubbed Modified Newtonian Dynamics (MOND) [16]. However, this theory faces significant challenges, such as violations of conservation laws, predictions of superluminal scalar waves, and an inability to explain certain cosmological observations – most notably, the Bullet Cluster and CMB. To address some of these issues, revised versions of MOND have since been developed, the most notable being Tensor-Vector-Scalar gravity (TeVeS) [17]. However, TeVeS still struggles to account for some key observations, such as those of the Bullet Cluster. While these models have not been entirely ruled out, it remains uncertain whether future modifications of TeVeS could

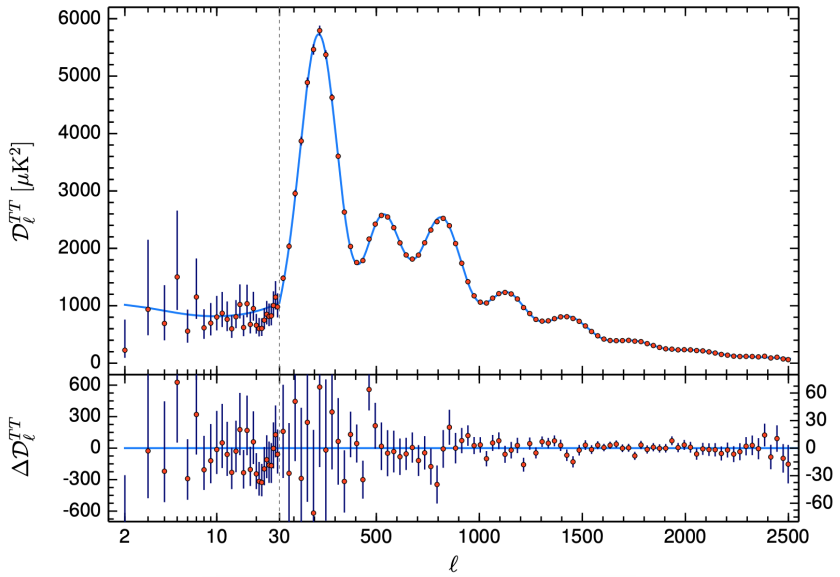

Figure 2.3: Cosmic microwave background temperature power spectrum, measured by Planck [4]. The light blue line in the above panel shows the base-ΛCDM theoretical spectrum fit. The lower panel shows the residuals with respect to this model. Figure credit: [4]

reconcile with current cosmological data [5]. As a result, the case for DM remains strong.

2.2 Origins of Dark Matter

Based on cosmological observations, such as the CMB, the abundance of DM in the universe can be estimated. This naturally raises the question: Where does this DM originate? Several mechanisms have been proposed to explain its production, with two of the most prominent being freeze-out and freeze-in, both occurring in the early universe [18].

2.2.1 Freeze-Out Mechanism

In the freeze-out scenario, DM particles were initially in thermal equilibrium with the hot plasma of the early universe. At high temperatures and number densities, frequent interactions maintained this equilibrium. As the universe expanded and cooled below the DM particle mass m_χ, DM annihilation processes became more prominent, leading to an exponential decrease in the equilibrium abundance [19].

Eventually, the temperature dropped to the point where the interaction rate fell below the expansion rate of the universe. At this stage, DM particles could no longer efficiently annihilate, and their abundance per comoving volume effectively froze out – becoming nearly constant. This freeze-out abundance, illustrated by the dashed orange curve in Figure 2.4, is approximately inversely proportional to the

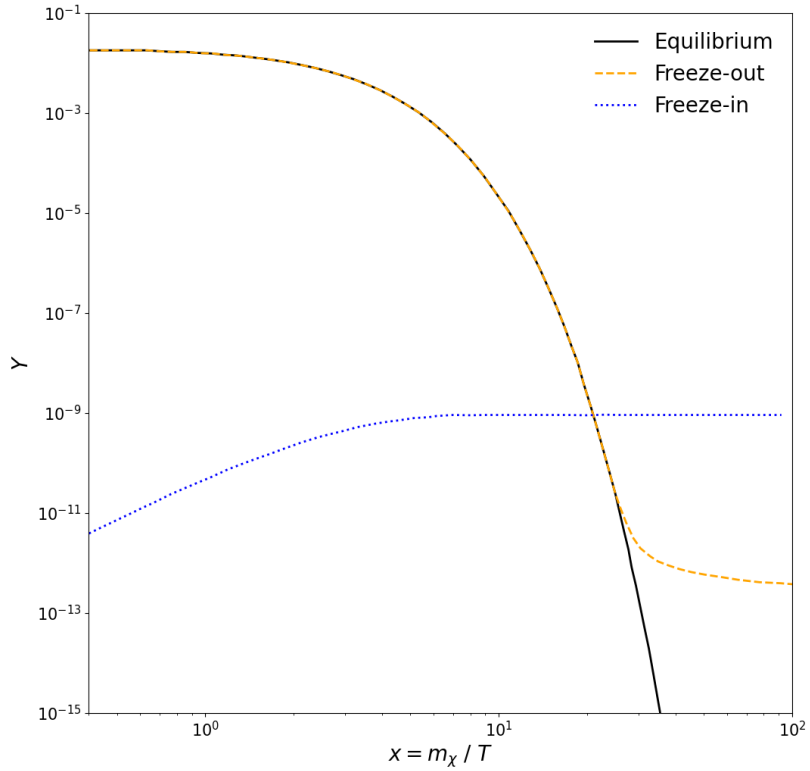

Figure 2.4: Evolution of the relic yield as the universe expanded and cooled for the freeze-out (dashed orange line) and freeze-in (dotted blue line) scenarios as a function of $x = m_\chi/T$, where m_χ is the dark matter mass, T is the temperature, and both axes are logarithmically scaled. The solid line represents the thermal equilibrium yield. Results are shown for a generic, nonzero coupling strength. This figure is derived from Figure 1 in [18].

thermally averaged annihilation cross section. This mechanism can, in certain DM models, account for the relic density observed in the universe today [19].

2.2.2 Freeze-In Mechanism

The freeze-in scenario follows a similar principle to freeze-out but assumes an extremely weak interaction between DM and the thermal plasma. Unlike in freeze-out, DM was never in thermal equilibrium due to these feeble interactions with Standard Model particles. Instead, its abundance gradually accumulated over time as the universe expanded and cooled. This process continued until production interactions became exceedingly rare, at which point the DM abundance stabilized, remaining frozen-in at its final relic value [18], see the dotted blue freeze-in curve in Figure 2.4.

2.3 Light Dark Matter

Thus far, an overview of the history, evidence, and early universe production mechanisms for DM has been provided, where "dark matter" has been treated in a very general way. In this section, the specific models of DM that form the focus of this thesis will be introduced.

The mass spectrum of viable DM candidates spans an enormous range. At the lower end, ultralight DM with masses as small as[1] $\sim 10^{-21}$ eV [20] can exhibit wave-like behavior on galactic scales [21]. At the opposite end lie extremely heavy candidates, such as the so-called "WIMPzilla" – a term humorously blending the prevalent "WIMP" (weakly interacting massive particle) DM model with "Godzilla" to underscore its massiveness – able to have a mass up to 10^{16} GeV [22, 23]. Even more massive non-particle candidates exist, such as primordial black holes, possibly weighing as much as $10M_{\odot}$ (solar masses) [24].

By assuming a thermal freeze-out origin for DM, this vast range becomes significantly narrower. Cosmological constraints, particularly from Big Bang Nucleosynthesis (BBN), place a lower bound on the DM mass near 1 MeV [25]. Meanwhile, unitarity limits on the DM annihilation cross section in the early universe impose an upper bound of a few hundred TeV [26].

Over the past few decades, substantial experimental efforts have focused on probing the GeV to multi-TeV range, which corresponds to the typical mass range of weakly interacting massive particles (WIMPs). This class of DM models has been particularly compelling, as WIMPs naturally reproduce the observed relic abundance via the thermal freeze-out mechanism – assuming electroweak-scale masses and interaction strengths of order unity. Despite the extensive searches, no conclusive detection has been made. These null results have placed increasingly stringent constraints on the parameter space for these models. While this space is not fully excluded and the WIMP remains a well-motivated and credible candidate, the lack of detection has prompted growing interest in alternative DM scenarios that lie outside the traditional WIMP mass window [6, 21, 27].

Among these alternatives is light dark matter (LDM), which may have evaded direct detection at nuclear recoil experiments thus far due to its mass being below that of the nucleons. To account for the correct observed relic abundance, LDM candidates must interact through a new force, with a corresponding new mediator serving as a portal between the hidden and visible sectors. These light candidates, if assumed to be thermal[2], cover masses from roughly the MeV to GeV scale – a range that remains well-motivated as it can yield the correct relic abundance via mechanisms like freeze-out, while still evading current cosmological constraints and experimental bounds [6, 28, 29].

[1] Throughout this thesis, natural units are used.

[2] Thermal DM refers to DM that once was in thermal equilibrium with the hot plasma of the early universe.

2.3.1 Cosmological Constraints

In the thermal freeze-out scenario, the relic abundance of DM is determined by its annihilation rate in the early universe. Matching the observed relic density imposes constraints on this rate during freeze-out [19]. At later times, observations of the CMB, measured by Planck [4], place stringent limits on DM annihilation into Standard Model particles during the cosmic dark ages – the period after the CMB was emitted but before the first stars were formed [30]. Annihilation during this epoch injects energy into the intergalactic medium (IGM), altering the ionization history of the universe and leaving an observable imprint on the CMB [31, 32].

In the non-relativistic regime, the DM annihilation cross section can be expanded in powers of the relative velocity v_{rel} between annihilating DM particles [31, 33, 34]:

$$\sigma v_{rel} = \underbrace{a}_{s-\text{wave}} + \underbrace{b v_{rel}^2}_{p-\text{wave}} + \mathcal{O}(v_{rel}^4). \tag{2.1}$$

Here, the leading term a corresponds to s-wave annihilation, which is velocity independent and thus remains active from freeze-out to the present epoch. The second term bv_{rel}^2, corresponding to p-wave annihilation, becomes highly suppressed at low velocities.

Planck measurements constrain the total power injected by DM annihilation during the cosmic dark ages, captured by the effective parameter:

$$p_{\text{ann}} = f_{\text{eff}} \frac{\langle \sigma v_{rel} \rangle_{\text{CDA}}}{m_{DM}} < 3.2 \times 10^{-28} \text{cm}^3 \text{s}^{-1} \text{GeV}^{-1}, \tag{2.2}$$

where f_{eff} is the fraction of annihilation energy deposited into the IGM, $\langle \sigma v_{rel} \rangle_{\text{CDA}}$ is the thermally averaged annihilation cross section during the cosmic dark ages, and m_{DM} is the DM mass [4]. As the value $f_{\text{eff}} \sim 0.15 - 1$ for typical annihilation channels [6], the constraint on the annihilation cross section becomes:

$$\langle \sigma v_{rel} \rangle_{\text{CDA}} \lesssim m_{DM} \times 10^{-27} \text{cm}^3 \text{s}^{-1} \text{GeV}^{-1}. \tag{2.3}$$

For s-wave annihilation, the required cross section at freeze-out is approximately $\langle \sigma v_{rel} \rangle_{\text{FO}} \sim 3 \times 10^{-26} \text{cm}^3 \text{s}^{-1}$ [31]. Given its velocity independence, this implies $\langle \sigma v_{rel} \rangle_{\text{CDA}} \simeq \langle \sigma v_{rel} \rangle_{\text{FO}}$, making s-wave dominated thermal relics strongly constrained by the CMB[3]. Specifically, such models are challenging to reconcile with observations for DM masses below ~ 10 GeV [32].

[3]These bounds may be evaded in scenarios where the annihilation rate is suppressed by alternative mechanisms, such as in asymmetric DM models – where an excess of DM particles over antiparticles reduces annihilation interactions [32] – or in non-thermal production scenarios that do not rely on thermal freeze-out to generate the relic abundance. Another alternative is resonant enhancement of the annihilation cross section during the early universe – requiring the tight relation $2 < m_{A'}/m_\chi \lesssim 2.5$ [35].

In contrast, p-wave annihilation requires $\langle \sigma v_{rel} \rangle_{\mathrm{FO}} \sim 6 \times 10^{-26} \mathrm{cm}^3 \mathrm{s}^{-1}$ at freeze-out [31], but is strongly suppressed at late times due to the v^2 scaling. As a result, such models naturally evade this CMB constraint while still achieving the observed relic abundance via thermal freeze-out [6].

2.3.2 Vector Portal – The Dark Photon

This thesis focuses on a class of models in which interactions between the dark sector and SM particles are mediated through the vector portal, with the dark photon serving as the mediator. The dark photon is assumed to be massive either due to the spontaneous breaking of a new dark gauge symmetry $U(1)'$, or via the Stueckelberg mechanism, which does not require the new $U(1)'$ symmetry to be spontaneously broken. Interaction with SM particles arises through kinetic mixing with the SM photon, characterized by a small dimensionless mixing parameter ϵ. This mixing enables the dark photon to weakly interact with SM particles, thereby providing a link between the dark and visible sectors [36].

The relevant terms of the Lagrangian describing the dynamics of the dark photon A'_μ, including its interaction with DM χ and the effective interaction terms stemming from kinetic mixing with the SM photon, can be expressed as [29, 37]:

$$\mathcal{L} \supset \mathcal{L}_\chi - \frac{1}{4} F'_{\mu\nu} F'^{\mu\nu} + \frac{m^2_{A'}}{2} A'_\mu A'^\mu - A'_\mu J^\mu_{EM} + A'_\mu J^\mu_\chi, \tag{2.4}$$

where $F'_{\mu\nu} = \partial_\mu A'_\nu - \partial_\nu A'_\mu$ is the field strength tensor for the dark photon, $\mathcal{L}_\chi$ contains the non-interaction DM terms, $m_{A'}$ is the dark photon mass, and the term J^μ_χ denotes the DM current. The electromagnetic current is defined as:

$$J^\mu_{EM} = e\epsilon \sum_f Q_f \bar{\psi}_f \gamma^\mu \psi_f, \tag{2.5}$$

where the sum runs over SM fermions f, and Q_f is their respective electric charge.

This framework allows for a range of DM candidates. In this thesis, three scenarios will be considered: Complex scalar, Dirac fermion, and Majorana fermion candidates. The pseudo-Dirac fermion model, often discussed in the literature, is left for future work.

Complex Scalar Dark Matter

In this scenario, the DM candidate is a complex scalar field χ with mass m_χ. The relevant terms in the Lagrangian and the associated current are given by:

$$\mathcal{L}_\chi = \frac{1}{2} \partial_\mu \chi^\dagger \partial^\mu \chi - m^2_\chi \chi^\dagger \chi, \tag{2.6}$$

$$J^\mu_\chi = i g_D [\chi^\dagger \partial^\mu \chi - (\partial^\mu \chi^\dagger) \chi], \tag{2.7}$$

where g_D is the $U(1)'$ gauge coupling. It is common to define the dark-sector analogue of the fine-structure constant as $\alpha_D \equiv \frac{g_D^2}{4\pi}$.

The annihilation cross sections into light SM leptons ($m_\chi \gg m_\ell$) and hadrons via a dark photon are given by [38]:

$$\sigma v_{rel}(\chi\chi^\dagger \to \ell^+\ell^-) \simeq \frac{8\pi\alpha v_{rel}^2}{3}\frac{y}{m_\chi^2}, \tag{2.8}$$

$$\sigma v_{rel}(\chi\chi^\dagger \to (\text{hadrons})) \simeq R(s) \times \sigma v_{rel}(\chi\chi^\dagger \to \mu^+\mu^-), \tag{2.9}$$

given that $2m_\chi < m_{A'}$. Here, $\alpha \equiv \frac{e^2}{4\pi}$ is the ordinary fine-structure constant, and the decays into hadrons are accounted for utilizing the R-ratio from experiments [39]:

$$R(s) \equiv \frac{\sigma_{tot}(e^+e^- \to \text{hadrons})}{\sigma(e^+e^- \to \mu^+\mu^-)}, \tag{2.10}$$

The dimensionless parameter y encapsulates the relevant model parameters:

$$y \equiv \epsilon^2\alpha_D\left(\frac{m_\chi}{m_{A'}}\right)^4, \tag{2.11}$$

and is widely used in exclusion plots in the (m_χ, y) plane, allowing for direct comparison to thermal targets – the region of parameter space where the observed DM abundance is correctly obtained via thermal freeze-out [29, 37, 40].

As seen in Eqs. 2.8 and 2.9, annihilation in this model is p-wave dominated, which significantly weakens the exotic energy injection constraints from the CMB, discussed in Section 2.3.1.

Dirac Fermion Dark Matter

In this model, the DM candidate is a Dirac fermion with a distinct antiparticle. The corresponding Lagrangian and current are:

$$\mathcal{L}_\chi = i\bar{\chi}\gamma^\mu\partial_\mu\chi - m_\chi\bar{\chi}\chi, \tag{2.12}$$

$$J_\chi^\mu = \bar{\chi}(g_D^V + g_D^A\gamma^5)\gamma^\mu\chi. \tag{2.13}$$

Here, g_D^V and g_D^A denote the vector and axial-vector couplings, respectively. In this work, $g_D^A = 0$ is used for the Dirac fermion dark matter model. Beyond simplicity, this choice also avoids the need for additional model ingredients – such as a dark Higgs – to preserve perturbative unitarity at high energies [41, 42]. In this work, the dark-sector analogue of the fine-structure constant is defined as $\alpha_D = \frac{(g_D^V)^2}{4\pi}$ for this model.

The annihilation cross section for the Dirac fermion model is s-wave dominated, as seen by the absence of velocity suppression [38, 43]:

$$\langle \sigma v_{rel} \rangle_{\text{ann}} \sim \frac{\alpha y}{m_\chi^2}. \tag{2.14}$$

As a result, stringent constraints apply, as discussed in Section 2.3.1. Consequently, Dirac fermion models are often disfavored and rarely featured in the literature. Nonetheless, this scenario is included here for completeness and comparison, given its structural similarity to other well-motivated candidates.

Majorana Fermion Dark Matter

This scenario closely resembles the Dirac case but assumes that the DM candidate is a Majorana fermion – its own antiparticle. The relevant Lagrangian and current are [44]:

$$\mathcal{L}_\chi = \frac{i}{2}\bar{\chi}\gamma^\mu \partial_\mu \chi - \frac{1}{2} m_\chi \bar{\chi}\chi, \tag{2.15}$$

$$J_\chi^\mu = \frac{1}{2}\bar{\chi}(g_D^V + g_D^A \gamma^5)\gamma^\mu \chi. \tag{2.16}$$

Due to the Majorana nature of χ, the bilinear $\bar{\chi}\gamma^\mu\chi$ identically vanishes. Hence, only the axial-vector coupling contributes to its interactions, and therefore $g_D^A \neq 0$ is used in this model. The dark-sector analogue of the fine-structure constant is here defined as $\alpha_D = \frac{(g_D^A)^2}{4\pi}$. Some further details on the vector current suppression are provided in Appendix A.

The annihilation cross section in this model turns out to be the same as in the complex scalar case [38]:

$$\sigma v_{rel}(\chi\chi \to \ell^+\ell^-) \simeq \frac{8\pi\alpha v_{rel}^2}{3}\frac{y}{m_\chi^2}, \tag{2.17}$$

$$\sigma v_{rel}(\chi\chi \to (\text{hadrons})) \simeq R(s) \times \sigma v_{rel}(\chi\chi \to \mu^+\mu^-), \tag{2.18}$$

meaning annihilation is p-wave dominated, and the associated velocity suppression alleviates the CMB constraints described in Section 2.3.1, thereby maintaining the Majorana fermion as a well-motivated DM candidate.

Model Parameters

The parameters governing these models are:

$$(m_{A'}, m_\chi, \epsilon, \alpha_D). \tag{2.19}$$

In this thesis, the following common benchmark is adopted:

$$m_{A'} = 3m_\chi, \qquad \alpha_D = 0.1. \tag{2.20}$$

This reduces the effective parameter space to two dimensions – for example, (m_χ, y) – facilitating clearer visual representation of experimental sensitivities and thermal relic targets.

2.3.3 Dark Sector Searches

Light DM models featuring an associated dark sector mediator – typically the dark photon – have become increasingly popular in physics beyond the Standard Model. In addition to strong constraints from cosmological observations, a broad array of terrestrial experiments have probed this scenario, placing increasingly stringent limits on mass and interaction strengths [36]. This section outlines the primary strategies used in dark sector searches – applicable not only to light DM models – and highlights some notable experiments.

Search Strategies

Dark sector searches can be broadly categorized into three complementary approaches: direct detection, indirect detection, and accelerator-based experiments. In practice, a combination of signals from multiple search strategies would be required to confirm and characterize a DM discovery [45, 46].

Direct detection searches rely on DM particles from the galactic halo intersecting with detector materials on Earth as the planet moves through the galaxy [47]. When such an encounter occurs, a DM particle χ may scatter off a nucleus or particle P in the detector – for example an electron – via the process $\chi P \to \chi P$, potentially generating a detectable recoil signal [48].

Indirect detection searches focus on astrophysical regions where DM is expected to accumulate due to gravitational attraction, such as galactic centers, stars, or even the Earth. In these dense regions, the probability of DM decay or self-annihilation events – such as $\chi\bar{\chi} \to \gamma\gamma, \gamma Z, q\bar{q}, e^+e^-$, or W^-W^+ – increases, leading to production of Standard Model particles which can then be detected [48].

Accelerator-based experiments aim to produce DM in high-energy collisions, such as $pp \to \chi\bar{\chi} + X$, where X denotes visible Standard Model products [48]. A primary detection strategy – employed in experiments like LDMX [28] – involves precision measurements of the energy or momentum of both incoming and outgoing particles. If DM is produced and escapes undetected, taking with it energy and momentum, its presence can be inferred by the resulting energy or momentum imbalance. Additional techniques include searching for scattering of produced DM within a detector or detecting visible decay products if the dark sector mediator is unstable [49].

Experimental Landscape

The **E137** experiment at the Stanford Linear Accelerator Center (SLAC) was a beam dump experiment[4] using a 20 GeV electron beam incident on an aluminum target. Originally designed to search for long-lived neutral particles such as "generic

[4] A beam dump experiment is a type of fixed-target experiment characterized by a thick and dense target, meaning that while all beam dump experiments are fixed-target setups, the converse does not necessarily hold.

axions" and "photinos" [50], the data have since been reanalyzed to constrain sub-GeV DM scenarios [51].

BaBar, an asymmetric e^+e^- collider at SLAC operating at a center-of-mass energy of 10.58 GeV, was designed to study *CP*-violation in B meson decays [52]. Subsequent analyses of BaBar data have searched for dark photon signatures, placing firm limits across a mass range from 20 MeV to over 10 GeV [53].

The **MiniBooNE** experiment, originally designed to study neutrino oscillations using an 8 GeV proton beam in a beam dump configuration, was later leveraged to conduct a dedicated search for light DM. This extended use of the existing setup enabled MiniBooNE to probe potential DM signatures alongside its primary neutrino program [54, 55].

The **NA64** fixed-target experiment at the CERN Super-Proton-Synchrotron (SPS) searches for dark photons produced in electron–nucleus collisions, using a 100 GeV electron beam directed at a stationary target. By analyzing missing energy events, NA64 has placed stringent new constraints on the parameter space of dark photon models [56].

The **Light Dark Matter eXperiment (LDMX)** is a planned fixed-target experiment specifically designed to probe the parameter space of thermal light DM through precision measurements of missing momentum. In its first phase, utilizing a 4 GeV electron beam, LDMX is expected to significantly surpass the sensitivity of previous DM searches over a range of masses. The planned second phase, featuring an upgraded 8 GeV electron beam, will extend its sensitivity even further, offering deeper insight into light DM scenarios [28].

Beyond the major efforts discussed above, a diverse range of other experiments also play an important role in probing the dark sector. Notable examples include **Belle II** [57], **DUNE** [58], and **LSND** [59, 60]. This list is by no means exhaustive, as ongoing and upcoming searches across a broad experimental landscape continue to probe the light DM scenario.

2.4 SHiP – Search for Hidden Particles

Adding to the landscape of terrestrial DM searches, the SHiP experiment is a recently approved general-purpose experiment to be built at the CERN SPS. Unlike high-energy collider experiments that operate at the energy frontier, SHiP is a beam dump experiment designed to operate at the intensity frontier. By directing a high-intensity proton beam onto a dense target, SHiP will produce a large flux of secondary particles, creating ideal conditions for studying rare processes and weakly interacting particles. The experiment will perform a wide neutrino physics program and also provides great capabilities for light DM searches [61]. An overview of the planned experimental setup can be seen in Figure 2.5.

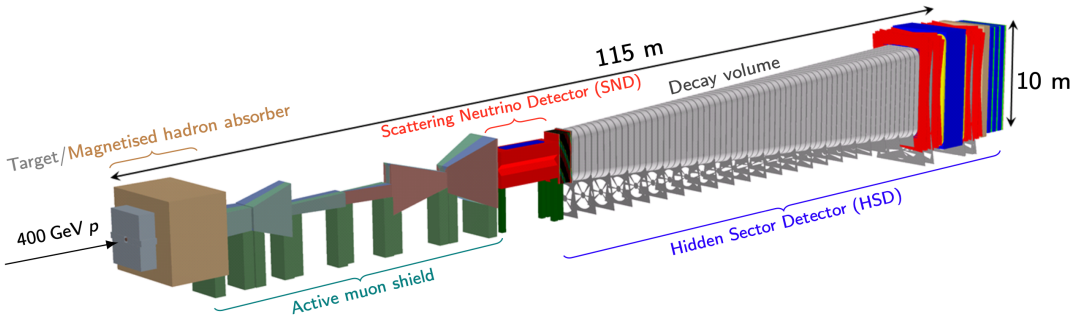

Figure 2.5: Overview of the SHiP experimental setup. Figure credit: [29]

In short, a 400 GeV proton beam is delivered onto a thick target made of blocks of a titanium-zirconium doped molybdenum alloy followed by blocks of tungsten[5]. This results in a total of 2×10^{20} protons on target (POT) over its 5 year operation period [29, 61]. Following the target, a hadron stopper consisting of a thick iron shielding is used. Additionally, a muon shield, utilizing a series of magnets to divert muons away from the downstream detectors, is also used to make as clean a flux as possible of neutrinos and hidden sector particles [29, 63].

The experiment features two complementary detectors: the Scattering Neutrino Detector (SND) and the Hidden Sector Detector (HSD). Positioned at the end of the setup, the HSD includes a long decay volume where long-lived hidden sector particles can decay into visible sector particles. This system integrates a spectrometer, a calorimeter, and a background tagging mechanism to reconstruct the decay vertices of these particles. However, in the search for light DM, the detector of interest is the SND [29, 61].

The SHiP SND combines dense passive material – enhancing interaction probability – with sub-micrometer position resolution and milliradian angular resolution. This allows it to detect light DM through scattering interactions with electrons or nuclei inside the detector, making this setting of the SHiP experiment a direct detection search. Such LDM scattering events, $\chi e^- \to \chi e^-$, can produce electromagnetic showers that are typically distinguishable from neutrino-induced events, which more often result in a range of different particles. Nonetheless, some background remains – particularly from neutrino interactions mimicking the LDM signature [29, 61].

Table 2.1 summarizes the overall geometry of the SHiP experiment as used in the simulations and analysis presented in this thesis. Additionally, detector efficiency unity is adopted, as in [29]. The configuration adopted here corresponds to the ECN4 layout of the SHiP experiment, consistent with the approach taken in [29]. It should be noted that another design – the ECN3 configuration – has recently been approved as the final setup [64]. This version features modifications such as a reduced target-detector distance, a change in the target material, and more protons

[5]Consistent with some previous studies (e.g., [62]), the target is modeled in simulations as a uniform block composed of molybdenum, the primary interaction material, for simplicity.

Table 2.1: Key parameters of the SHiP experiment setup used in simulations. Values and references are provided for the proton beam, target, and detector. The detector position is specified relative to the center of the beam dump target, with the z-axis oriented along the beam direction.

Proton Beam [29]	Total POT	Energy		
	2×10^{20}	400 GeV		
Target [29, 66]	Material	Length		
	^{96}Mo	1.2 m		
Detector Position [29, 65]	x-pos	y-pos	z-pos	
	0 m	0 m	38 m	
Detector [29, 67]	Material	Width	Height	Length
	^{207}Pb	0.9 m	0.75 m	3.21 m

on target due to a longer operation period. For more details, readers are referred to [65] and references therein. Nevertheless, the ECN4 setup is retained in this work to ensure consistency and direct comparability with the results and methodology of previous studies, particularly those presented in [29].

2.4.1 Dark Photon Production Mechanisms

In general, the main production mechanisms for dark photons include [36]:

- Bremsstrahlung (Figures 2.6a and 2.6b): An incoming charged particle (e.g., a proton) scatters off some target (e.g., a proton or nucleus). In this scattering process, the charged particle can emit a dark photon: $pN \to pNA'$.

- Annihilation (Figure 2.6c): An electron-positron pair annihilates into an ordinary and a dark photon: $e^-e^+ \to \gamma A'$.

- Meson decays (Figure 2.6d): A meson $\mathbf{m}$ decays, producing an ordinary and a dark photon: $\mathbf{m} \to \gamma A'$.

- Drell-Yan (Figure 2.6e): A quark-antiquark pair annihilates into a dark photon: $q\bar{q} \to A'$.

At proton beam dumps, this list is narrowed down to proton bremsstrahlung, meson decays, and Drell-Yan production. Among the meson decay channels, the π^0 and η mesons are the most relevant due to their relatively large branching ratios into photons. Drell-Yan production, on the other hand, has been found to be subdominant at SHiP for the mass range considered here [29]. Consequently, the three dark photon production channels considered in this work are π^0 decay, η decay, and

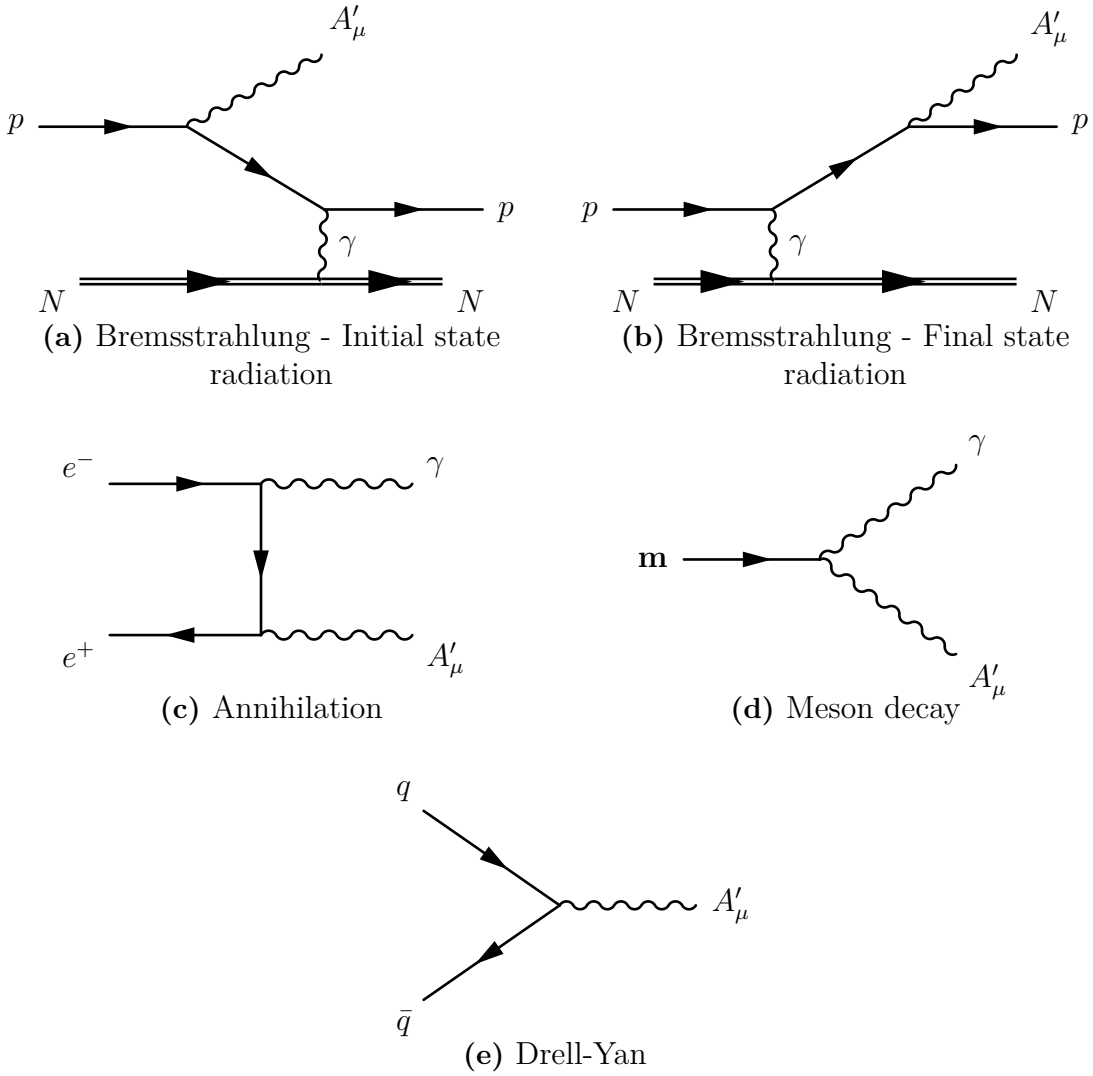

(a) Bremsstrahlung - Initial state radiation

(b) Bremsstrahlung - Final state radiation

(c) Annihilation

(d) Meson decay

(e) Drell-Yan

Figure 2.6: Dark photon production through proton bremsstrahlung (a) and (b), electron-positron annihilation (c), meson decay (d), and the Drell-Yan process (e).

proton bremsstrahlung.

Proton Bremsstrahlung

Bremsstrahlung is a significant production mechanism not only in the context of dark photon generation in proton beam experiments but also in electron beam setups and the production of various other particles. Due to the inherent complexity of such processes, approximations can be employed to increase simplicity and reduce computational demand [68].

A famous approach is the Weizsäcker-Williams approximation, which exploits the fact that in the rest frame of an incoming particle, the electromagnetic field of a rapid target nucleus behaves similarly to a flux of virtual photons [69]. Originally applied to bremsstrahlung processes in [70, 71], this approximation allows the differential cross section of the full $2 \to 3$ process – such as $ep \to epA'$ – to be related to the simpler $2 \to 2$ subprocess $e\gamma \to eA'$ [68].

A similar approach was later proposed by Blümlein and Brunner [72]. In their formulation, the full $pp \to ppA'$ process is first expressed in terms of the subprocess $pb \to pA'$, where b denotes a virtual vector boson exchanged between the beam and target protons. Taking the four-momentum of b to zero, the process is then related to the $1 \to 2$ splitting process $p \to pA'$ via a splitting function $w_{pA'}(z, p_T^2)$ [73]:

$$\left[\frac{d^2\sigma(pp \to ppA')}{dz dp_T^2}\right]_{BB} = w_{pA'}(z, p_T^2)\sigma_{pp}(s'). \tag{2.21}$$

Here, p_T is the transverse momentum of the emitted dark photon and $z \equiv p_z/P_z$ is the fraction of the incoming proton's longitudinal momentum P_z carried away by the outgoing dark photon. Furthermore, $\sigma_{pp}(s')$ is the elastic proton-proton scattering cross section taken in the reduced center-of-mass energy squared $s' = 2m_p(E_p - E_{A'})$, with m_p the proton mass, E_p the beam energy, and $E_{A'}$ the dark photon energy [73, 74].

The splitting function derived by Blümlein and Brunner takes the form [72]:

$$w_{pA'}(z, p_T^2) = \frac{\epsilon^2\alpha}{2\pi H}\left\{\frac{1+(1-z)^2}{z} - 2z(1-z)\left[\frac{2m_p^2 + m_{A'}^2}{H}\right.\right. \tag{2.22}$$
$$\left.\left. -2\left(\frac{z \cdot m_p^2}{H}\right)^2\right] + 2z(1-z)\Big[1+(1-z)^2\Big]\left(\frac{m_p m_{A'}}{H}\right)^2 + 2z\left(\frac{(1-z)m_{A'}^2}{H}\right)^2\right\},$$

with the kinematic structure function [75]:

$$H = p_T^2 + (1-z)m_{A'}^2 + (zm_p)^2. \tag{2.23}$$

For the derivation of this splitting function to be valid, the following kinematic conditions must be satisfied [72]:

$$E_p, E_{A'}, E_p - E_{A'} \gg m_p, m_{A'}, |p_T|. \tag{2.24}$$

The differential dark photon production rate per proton interaction is then given by [74]:

$$\frac{d^2N}{dzdp_T^2} = \frac{\sigma_{pp}(s')}{\sigma_{pp}(s)} w_{pA'}(z, p_T^2), \tag{2.25}$$

where $s = 2m_pE_p$ is the center-of-mass energy squared. This expression applies not only for proton-proton bremsstrahlung, but also for hadronic targets A, as the hadronic cross section can be factorized as $\sigma_{pA}(s) = f(A)\sigma_{pp}(s)$, where the function $f(A)$ – depending only on the atomic number of A – cancels in the ratio [74].

Finally, the total production rate of dark photons per proton interaction can be obtained by integrating over the relevant phase space, z and p_T^2. Keeping in mind that the conditions of Eq. 2.24 must be satisfied, appropriate limits in the setting of the SHiP experiment would be $z \in [0.1, 0.9]$ and $p_T^2 \in [0, 16]$ GeV [29].

Rare π^0 and η Decays

In the collisions of high-energy protons on heavy nuclear targets – such as those encountered in the SHiP experiment – a large number of mesons are produced [29]. Among these, the decay of π^0 and η mesons provides the dominant contributions to dark photon production in the lower parts of the dark photon mass range considered in this thesis [37].

Once a π^0 meson is produced, dark photons can be generated via the rare decays $\pi^0 \to \gamma A'$. The partial decay width for this process can be expressed relative to the decay $\pi^0 \to \gamma\gamma$ as follows [76]:

$$\frac{\Gamma(\pi^0 \to \gamma A')}{\Gamma(\pi^0 \to \gamma\gamma)} \simeq 2\epsilon^2 \left(1 - \frac{m_{A'}^2}{m_{\pi^0}^2}\right)^3, \tag{2.26}$$

valid in the dark photon mass range $m_{A'} < m_{\pi^0}$ (on-shell)[6]. The corresponding branching ratio[7] is given by:

$$\begin{aligned} BR(\pi^0 \to \gamma A') = \frac{\Gamma(\pi^0 \to \gamma A')}{\Gamma_{\pi^0}} \simeq 2\epsilon^2 \left(1 - \frac{m_{A'}^2}{m_{\pi^0}^2}\right)^3 \frac{\Gamma(\pi^0 \to \gamma\gamma)}{\Gamma_{\pi^0}} = \\ = 2\epsilon^2 \left(1 - \frac{m_{A'}^2}{m_{\pi^0}^2}\right)^3 BR(\pi^0 \to \gamma\gamma), \end{aligned} \tag{2.27}$$

where Γ_{π^0} is the total decay width of the π^0 meson. An analogous expression holds for the on-shell η decay channel ($m_{A'} < m_\eta$), giving [29]:

$$\frac{BR(\pi^0, \eta \to \gamma A')}{BR(\pi^0, \eta \to \gamma\gamma)} \simeq 2\epsilon^2 \left(1 - \frac{m_{A'}^2}{m_{\pi^0,\eta}^2}\right)^3, \tag{2.28}$$

[6] Only on-shell contributions are considered here, as the π^0 decay channel becomes subdominant well before $m_{A'} = m_{\pi^0}$, with similar behavior for the η channel [37].

[7] A branching ratio quantifies the likelihood of a particle decaying into a particular final state compared to all its possible decay channels.

where the branching ratios for the visible decays $\mathbf{m} \to \gamma\gamma$ are available from experimental data [77]:

$$BR(\mathbf{m} \to \gamma\gamma) \simeq \begin{cases} 98.8\% \ , \ \mathbf{m} = \pi^0. \\ 39.4\% \ , \ \mathbf{m} = \eta. \end{cases} \tag{2.29}$$

2.4.2 Dark Matter Production Mechanisms

Once a dark photon has been produced, it can decay visibly – into Standard Model particles – or invisibly, into dark sector particles, as illustrated in Figure 2.7. The partial decay widths for these processes are given by [36]:

$$\Gamma(A' \to l^+ l^-) = \frac{1}{3}\alpha\epsilon^2 m_{A'} \sqrt{1 - \frac{4m_l^2}{m_{A'}^2}} \left(1 + \frac{2m_l^2}{m_{A'}^2}\right), \tag{2.30}$$

$$\Gamma(A' \to (\text{hadrons})) = \frac{1}{3}\alpha\epsilon^2 m_{A'} \sqrt{1 - \frac{4m_\mu^2}{m_{A'}^2}} \left(1 + \frac{2m_\mu^2}{m_{A'}^2}\right) R(s = m_{A'}^2), \tag{2.31}$$

where decays into hadrons are accounted for utilizing the R-ratio from experiments [39] as defined in Eq. 2.10, and for decays to DM [41]:

$$\begin{aligned} \Gamma(A' \to \chi\chi^\dagger) &= \tfrac{\alpha_D m_{A'}}{12} \left(1 - \tfrac{4m_\chi^2}{m_{A'}^2}\right)^{3/2} && \text{(Complex Scalar)}, \\ \Gamma(A' \to \chi\bar{\chi}) &= \tfrac{\alpha_D m_{A'}}{3} \sqrt{1 - \tfrac{4m_\chi^2}{m_{A'}^2}} \left(1 + \tfrac{2m_\chi^2}{m_{A'}^2}\right) && \text{(Dirac Fermion)}, \\ \Gamma(A' \to \chi\bar{\chi}) &= \tfrac{\alpha_D m_{A'}}{3} \left(1 - \tfrac{4m_\chi^2}{m_{A'}^2}\right)^{3/2} && \text{(Majorana Fermion)}, \end{aligned} \tag{2.32}$$

where these expressions apply only when the decay is kinematically allowed ($m_{A'} > 2m_k$, $k = l, \mu, \chi$).

In the regime where the dark decay channel is open $m_{A'} > 2m_\chi$, and the dark-sector coupling dominates over the visible-sector coupling $\alpha_D \gg \alpha\epsilon^2$, the decays of dark photons are overwhelmingly into DM states [36][8]:

$$BR(A' \to \chi\bar{\chi}) \simeq 1. \tag{2.33}$$

These conditions are well satisfied for kinetic mixing values $\epsilon < 0.1$, with the earlier mentioned benchmark scenario for this thesis: $m_{A'} = 3m_\chi$ and $\alpha_D = 0.1$.

2.5 Detection Strategies

Even though the kinetic mixing parameter ϵ is taken to be small – implying weak interactions between DM and SM particles – the dark photon may still mediate

[8] In in Eq. 2.33, $\bar{\chi}$ denotes the antiparticle of χ and is used generically for both fermionic and complex scalar DM. This notation is used throughout the thesis, except when the complex scalar case is treated separately, in which case the more accurate notation $\chi^\dagger$ is used.

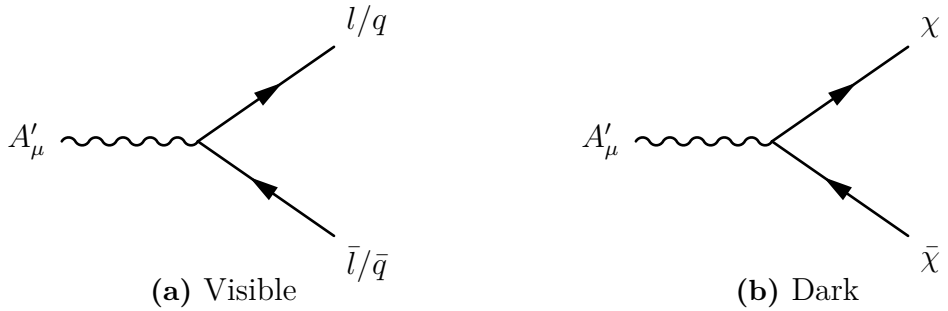

(a) Visible **(b)** Dark

Figure 2.7: Feynman diagrams of a dark photon decaying into SM leptons, hadrons, and dark matter.

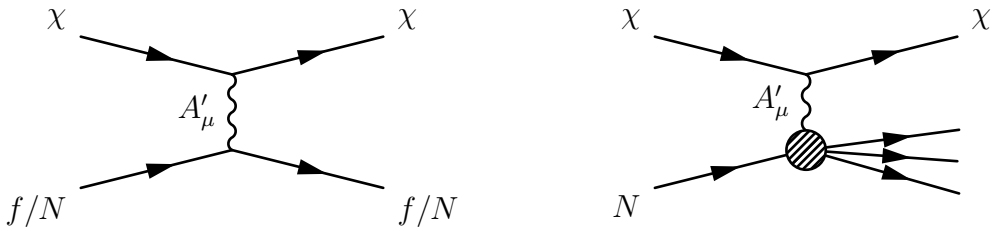

(a) Elastic scattering off of electrons or nucleons.

(b) Deep inelastic scattering off of nucleons.

Figure 2.8: Feynman diagrams of the relevant scattering channels for detection of dark matter in the SHiP experiment.

sufficiently strong interactions between them to enable DM detection. At SHiP, relevant detection channels for DM produced via dark photon decays include elastic scattering off electrons and nucleons (Figure 2.8a), as well as deep inelastic scattering off nucleons (Figure 2.8b), both mediated by dark photon exchange [37]. Among these, elastic scattering off electrons – partly because this channel is less plagued by background events – offers the highest sensitivity in the SHiP experiment [78], and will therefore be the focus in this work.

The differential cross sections for elastic scattering of DM off electrons in the three considered models take the forms [51, 79]:

$$\frac{d\sigma(\chi e^- \to \chi e^-)}{dE_e} = \frac{4\pi\alpha\alpha_D\epsilon^2}{(E_\chi^2 - m_\chi^2)(m_{A'}^2 + 2m_e E_e - 2m_e^2)^2} \times \tag{2.34}$$

$$\times \begin{cases} 2m_e E_\chi^2 - (2m_e E_\chi + m_\chi^2)(E_e - m_e) & \text{(Complex Scalar)}, \\ 2m_e E_\chi^2 - (2m_e E_\chi - m_e E_e + m_\chi^2 + 2m_e^2)(E_e - m_e) & \text{(Dirac Fermion)}, \\ 2m_e(E_\chi^2 - m_\chi^2) - (2m_e E_\chi - m_e E_e - m_\chi^2 + 2m_e^2)(E_e - m_e) & \text{(Majorana Fermion)}. \end{cases}$$

2.5.1 Comparison with Electron Beam Dump Experiments

In total, for a fixed mass point (m_χ, $m_{A'} = 3m_\chi$), the signal yield at SHiP scales as $\epsilon^4\alpha_D$ with the remaining model parameters. The ϵ^2 arises from the production of the dark photon, and the additional $\epsilon^2\alpha_D$ from DM detection via electron scattering. This contrasts with electron fixed-target experiments, which typically rely on missing

energy or momentum signatures rather than scattering for detection. In such setups, the signal yield scales with just ϵ^2, reflecting only dark photon production. While this may suggest greater sensitivity, proton beam dump experiments can at least partially recoup this through enhanced dark photon production due to their higher penetrating power and additional production from rare meson decays [29].

2.6 Motivation for Simulation Studies

Having established the theoretical and experimental context, the vastness of the search space and the importance of fully utilizing experimental capabilities should now be more apparent. To guide optimization of experimental setups to enhance their sensitivity to a broad range of theoretical models, simulation tools play a central role. They provide essential insight into production channels, detector responses, and the impact of the experiment's overall geometry.

However, the reliability of conclusions drawn from simulations depends critically on understanding the tools themselves, including their limitations and assumptions. This underscores the motivation for the first aim of this thesis: a comparative study of the two simulation tools introduced in the following section.

In addition to this methodological focus, the thesis also explores the two dark sector candidates – Majorana and Dirac fermions – which are newly considered in the context of the SHiP experiment, alongside the baseline complex scalar model. This study, therefore, contributes to understanding the extent to which SHiP can probe the parameter space of these models. These insights are valuable not only for SHiP but also for informing the strategies of future experiments, helping to avoid redundant searches and directing attention to unexplored regions of theoretical interest.

3
Methods

This chapter outlines the methodology underlying the results presented in this thesis, which include both a comparative study of the simulation tools **BdNMC** and **MadDump**[1], as well as sensitivity estimates for the SHiP experiment in probing new dark models. To establish a foundation for these analyses, the chapter begins with a review of the most relevant internal mechanics of the two simulation frameworks. This is followed by a detailed account of the specific workflows and procedures used throughout the thesis to generate and analyze the simulation results.

3.1 Simulation Frameworks

To give a clear and structured overview of the two simulation tools – **BdNMC** [37] and **MadDump** [78][2] – they are presented sequentially in the sections below. The key differences and methodological variations, including their impacts on the output, will be highlighted in the results and discussion chapters.

3.1.1 Description and Overall Methodology

BdNMC is a standalone Monte Carlo simulation tool specifically developed for modeling complex scalar LDM production and scattering in neutrino detectors, within the context of proton beam fixed-target experiments. It supports a range of configurations, including various target materials, experimental setups, and detector geometries [37].

MadDump, by contrast, is a plugin for the broader **MadGraph5_aMC@NLO** framework, which is designed to facilitate comprehensive studies in Standard Model and Beyond Standard Model phenomenology. **MadDump** is tailored to simulate scenarios in which dark sector particles are produced in beam dump experiments and either scatter or decay visibly in a downstream detector. Like **BdNMC**, **MadDump** allows for flexible configurations of targets, geometries, and detectors [78].

Both tools require a set of inputs at initialization, including the relevant production channels, setup geometry, and detector specification. The specific inputs relevant in

[1]The **BdNMC** and **MadDump** software packages are available at `https://github.com/pgdeniverville/BdNMC` and `https://launchpad.net/maddump` respectively.

[2]This study employs **BdNMC** version 3.2.2, **MadDump** trunk series revision 57, and **MadGraph5_aMC@NLO** version 2.6.7

this analysis, and how they are configured, will be detailed in Section 3.2.

Simulation Methodology – BdNMC

BdNMC begins by computing the expected yield of dark matter particles χ from each production channel. For instance, in the case of π^0 decay via $\pi^0 \to \gamma A' \to \gamma\chi\chi^\dagger$, the expected number of dark matter particles produced is:

$$N_\chi = \text{POT} \times N_{\pi^0/\text{POT}} \times BR(\pi^0 \to \gamma\chi\chi^\dagger), \tag{3.1}$$

where $N_{\pi^0/\text{POT}}$ is the average number of π^0 mesons produced per proton on target (POT), and BR denotes the branching ratio. After computing yields for all production channels, a channel is selected at random, with the selection probabilities weighted by its relative dark matter yield:

$$Pr(j) = \frac{N_\chi^j}{\sum\limits_k N_\chi^k}, \tag{3.2}$$

where N_χ^j denotes the yield from channel j, and the sum runs over all specified production channels.

Next, the four-momentum of the relevant particle in the chosen channel is generated either via rejection sampling or by iterating through a pre-generated momentum list. In the case of the π^0 decay production channel, this particle would be the π^0 meson itself. The particle would then be decayed in its rest frame to produce daughter particles $d1$ and $d2$. Their momenta are given by:

$$|\vec{p}_{d1}| = |\vec{p}_{d2}| = \frac{m_p}{2}\sqrt{\lambda(m_p, m_{d1}, m_{d2})}, \tag{3.3}$$

with

$$\lambda(m_p, m_{d1}, m_{d2}) = |m_p^2 + m_{d1}^2 + m_{d2}^2 - 2(m_p m_{d1} + m_p m_{d2} + m_{d1} m_{d2})|, \tag{3.4}$$

where m_p, m_{d1}, m_{d2} denotes the masses of the parent and daughter particles. The angular direction of $\vec{p}_{d1}$ in the rest frame of the decaying particle is uniformly sampled using $\theta \in [-\frac{\pi}{2}, \frac{\pi}{2}]$, $\varphi \in [0, 2\pi]$, giving:

$$\vec{p}_{d1} = |\vec{p}_{d1}| \cdot (\sin(\theta)\cos(\varphi), \sin(\theta)\sin(\varphi), \cos(\theta)), \tag{3.5}$$

$$\vec{p}_{d2} = -\vec{p}_{d1}. \tag{3.6}$$

This decay procedure is recursively applied until the final-state dark matter particles are produced. For example, in the π^0 decay channel, the steps are: sample π^0 four-momentum, decay π^0 to $\gamma A'$, decay A' to $\chi\chi^\dagger$.

Following particle generation, the code computes the trajectory of each dark matter particle and checks its intersection with the detector. If neither particle intersects the detector volume, the simulation returns to the channel selection step. If at least

one particle intersects, the probability of a scattering event occurring within the detector is evaluated. This is done by computing:

$$R = \frac{\sigma(E_i) L_i n}{\max(\sigma L n)}, \tag{3.7}$$

where $\sigma(E_i)$ is the interaction cross section for a dark matter particle of energy E_i, L_i is the intersection length of the particle trajectory with the detector volume, n is the number density of target particles (in this case electrons), and $\max(\sigma L n)$ is the maximum value encountered during a preliminary burn-in phase (used for normalization in rejection sampling).

Next, a random number is uniformly drawn $u \in [0, 1]$. If $R > u$, it is determined that a scattering interaction occurs. Otherwise, the dark matter particle is discarded. For successful interactions, the corresponding count for that production channel $ninteractions^i$ (where superscript i represents the production channel) is incremented by one. The final state kinematics are then obtained from rejection sampling based on the differential cross section for the interaction – for example, Eq. 2.34 in the case of electron scattering.

This process is repeated until a specified number of successful scattering events, *samplesize*, is reached. The number of attempts required, starting from the production channel selection, is denoted as *trials*. The estimated number of signal events from channel i is then calculated as:

$$N^i_{signal} = \frac{ninteractions^i}{trials} \cdot \max(\sigma L n) \cdot N^{tot}_{\chi} \cdot \epsilon_{\text{eff}}, \tag{3.8}$$

where $\frac{ninteractions^i}{trials}$ represents the relative frequency of scattering events from channel i, $\max(\sigma L n)$ returns the correct normalization after the rejection sampling, $N^{tot}_{\chi} = \sum_i N^i_{\chi}$ is the total number of dark matter particles produced for the given number of POT, and ϵ_{eff} is the detector efficiency (here taken as unity).

Simulation Methodology – MadDump

The simulation workflow in **MadDump** varies slightly depending on the production mechanism of the hidden sector particles. Certain production channels, such as Drell-Yan processes, can be simulated directly within **MadDump**. Others, particularly those involving hadronic decays, require external event generators like **Pythia** [80] to model the production of relevant intermediate particles. This separation allows for more accurate modeling of physical processes such as secondary particle cascades based on the user's needs, rather than relying on generic approximations.

While certain combinations of production modes can technically be included in a single simulation session, each channel is treated and simulated separately here for simplicity. Final results from different production channels can then be combined through post-processing.

In addition to experiment-specific settings and potential pre-generated particle fluxes, **MadDump** requires a definition of the underlying physical model. This is provided via a Universal FeynRules Output (UFO) file [81], which may be generated using the *Mathematica* package **FeynRules** [82]. The UFO file encodes all relevant particles, parameters (masses, couplings, etc.), and interaction vertices derived from the model Lagrangian. Using this input, **MadDump**, via the **MadGraph5_aMC@NLO** framework, can compute the necessary ingredients – such as decay widths and differential cross sections – for the simulation.

Once the initial particles are generated – either internally or via external tools – they are propagated through their decay chains until the hidden sector particle of interest is produced. The full decay history, including four-momenta of all intermediate states, is saved to an output file. For example, in the dark photon model considered in this thesis, a representative production channel is the decay $\pi^0 \to \gamma A'$, followed by $A' \to \chi\bar{\chi}$. In this case, the flux and kinematics of π^0 mesons are generated externally (e.g., via **Pythia**) and provided to **MadDump** in a standard format such as **HepMC** [83]. The decays are then performed using the **MadSpin** module [84], a part of the **MadGraph5_aMC@NLO** suite. An analysis of **MadSpin** is beyond the scope of this work.

After production, hidden sector particles are assumed to travel unimpaired until they reach (or miss) the detector. Their distribution is described by a flux function:

$$\phi(E, \vec{x}) = \frac{dn_{DM}}{dEd\vec{x}}, \tag{3.9}$$

where E is the dark matter energy, n_{DM} is the number of dark matter particles, and $\vec{x}$ represents the other relevant kinematic variables (e.g., angular direction, production point, etc.).

Detection occurs either via scattering with detector material or through decay into visible Standard Model particles. As previously mentioned, only detection through scattering processes are relevant in this thesis. For decay-based scenarios, the reader is referred to the **MadDump** documentation.

The cross section for detection via scattering is given by:

$$\sigma_D = \int dE \int d^n\vec{x}\phi(E, \vec{x})W(E, \vec{x})\hat{\sigma}_D(E), \tag{3.10}$$

where $\hat{\sigma}_D(E)$ is the partonic cross section, and $W(E, \vec{x})$ is a weight function encoding detector geometry and efficiency – penalizing particles with short track lengths inside the detector volume and excluding those that miss it altogether.

If the product $\phi(E, \vec{x})W(E, \vec{x})$ were known analytically, the integral could be evaluated directly, and samples could easily be drawn. However, only discrete samples of the flux are available from the production stage of the simulation. To work around this, the fact that $\hat{\sigma}_D$ only depends on the energy is exploited by considering:

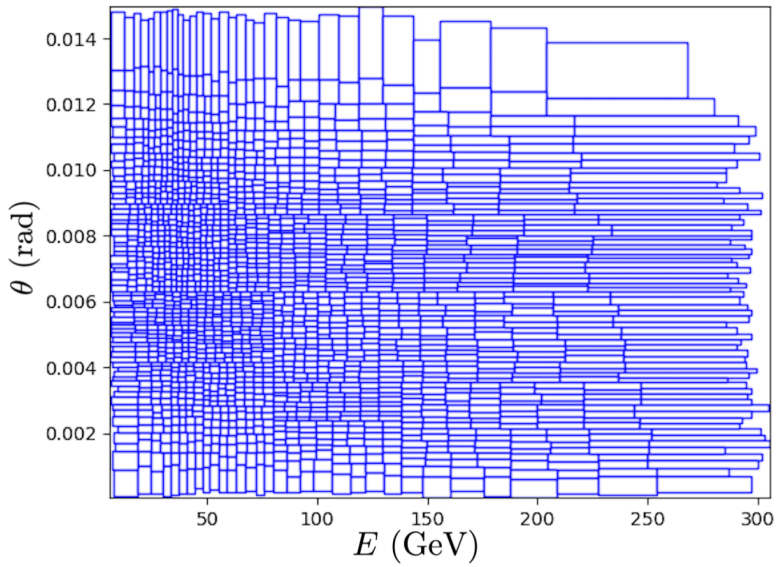

Figure 3.1: Example mesh from the two-dimensional fitting procedure for dark matter particles in **MadDump** [78].

$$\tilde{\phi}(E) = \int d^n\vec{x}\phi(E,\vec{x})W(E,\vec{x}), \tag{3.11}$$

which can be estimated via a one-dimensional fit to the production simulation samples representing $\phi(E,\vec{x})$. The total detection cross section σ_D can then be computed based on this fit, which in turn allows the estimated dark matter yield to be obtained. However, this does not allow for the full kinematic information of the scattered particles within the detector to be read out, which is crucial when analyzing experimental setups and selection cuts.

To this end, **MadDump** employs an additional fitting procedure. Assuming a point-like production region (justified by a small target length compared to the target-detector distance in typical fixed-target experiments), the relevant kinematics reduce to energy E, the polar angle θ, and the azimuthal angle φ, the latter two defined relative to the beam axis.

Furthermore, the production is assumed to be invariant under rotations about the beam axis, meaning φ has no correlations with E or θ and is only affected by detector geometry. This motivates a two-dimensional fit over (E,θ), which uses a binning strategy that adaptively partitions phase space so each bin contains an equal number of events. This creates bins with finer resolution in high-density regions, yielding a mesh that reflects the underlying distribution, an example of which is provided in Figure 3.1. For more details, see [78].

During event generation, samples are drawn from this two-dimensional distribution. For each sampled pair (E,θ), the allowed intervals of φ are determined based on the

detector geometry. These intervals correspond to the directions in which the particle would intersect the detector volume. In general, there may be multiple disjoint intervals for a fixed θ; for example, up to four in cubic geometries at sufficiently large values of θ. φ is then uniformly sampled from the union of these intervals, reconstructing the full incoming direction consistent with both the production distribution and the detector acceptance.

These incoming particles – now with fully characterized four-momenta – are then used to simulate scattering with the detector material. The resulting output includes the kinematic information for both incoming and scattered particles, enabling detailed event-level analyses and application of selection criteria to enhance the signal-to-background ratio.

3.1.2 Generation of π^0 and η Mesons

The default behavior of **BdNMC** is to use parametrized distributions for meson production. For the 9 GeV proton beam used in the MiniBooNE experiment [54], the **Sanford-Wang** distribution is recommended. However, for higher beam energies – such as the 400 GeV beam used in the SHiP experiment – the **BMPT** distribution [85] is more appropriate [37]. The following section provides an overview of the **BMPT** parametrization as implemented in **BdNMC**, beginning with π^0 meson production and subsequently extending to the η meson.

The **BMPT** framework gives the inclusive invariant differential cross section for meson production through the quantity:

$$E \times \frac{d^3\sigma}{dp^3}. \tag{3.12}$$

This differential cross section is initially fitted to experimental data from proton collisions with a specific target material and subsequently rescaled for application to other materials.

The **BMPT** parametrization is given by [85]:

$$E \times \frac{d^3\sigma}{dp^3} = A(1-x_R)^{\alpha}(1+Bx_R)x_R^{-\beta}(1+a'(x_R)p_T+b'(x_R)p_T^2)e^{-a'(x_R)p_T}, \tag{3.13}$$

where p_T is the transverse momentum of the produced particle, $x_R \equiv E^*/E^*_{\max}$ is the fraction of the actual and largest possible energy for the generated particle in the center-of-momentum frame, $a'(x_R) = a/x_R^{\gamma}$, and $b'(x_R) = a^2/(2x_R^{\delta})$.

These parameters are fitted to data from the NA20 and NA56/SPY experiments, which employed 400 and 450 GeV proton beams on beryllium targets, respectively [85]. The fit results for π^+ production are presented in Table 3.1.

To obtain the π^- spectrum, a parametrization of the π^+/π^- production ratio is introduced:

Table 3.1: Experimentally fitted values for $\pi^{\pm}$ inclusive production in proton-beryllium interactions as reported in [85].

A (mb/GeV^2)	B	α	β	a (GeV^{-1})	γ	δ	r_0	r_1
62.3	1.57	3.45	0.517	6.10	0.153	0.478	1.05	2.65

$$r_\pi = r_0(1 + x_R)^{r_1}, \tag{3.14}$$

where the fitted values for r_0 and r_1 are also found in Table 3.1.

Using this, the π^0 distribution is computed in **BdNMC** as the average of the π^+ and π^- spectra:

$$\begin{aligned}\left(E \times \frac{d^3\sigma}{dp^3}\right)_{\pi^0} &= \frac{1}{2}\left[\left(E \times \frac{d^3\sigma}{dp^3}\right)_{\pi^+} + \left(E \times \frac{d^3\sigma}{dp^3}\right)_{\pi^-}\right] = \\ &= \frac{1}{2}\left(E \times \frac{d^3\sigma}{dp^3}\right)_{\pi^+}\left(1 + \frac{1}{r_\pi}\right).\end{aligned} \tag{3.15}$$

To account for target materials other than the beryllium in the original target, the differential cross section is rescaled by:

$$E\frac{d^3\sigma^{pA_{target}}}{dp^3} = \left(\frac{A_{target}}{A_{Be}}\right)^{\alpha(x_F)} \cdot E\frac{d^3\sigma^{pA_{Be}}}{dp^3}. \tag{3.16}$$

Here, A_{target} and A_{Be} denote the mass numbers of the new target and beryllium, respectively. The scaling exponent $\alpha(x_F)$ is given by:

$$\alpha(x_F) = (0.74 - 0.55x_F + 0.26x_F^2) \cdot (0.98 + 0.21p_T^2), \tag{3.17}$$

where $x_F \equiv 2p_L^*/\sqrt{s}$, with p_L^* the longitudinal momentum of the produced particle and $\sqrt{s}$ the total energy, both in the center-of-momentum frame.

Once the differential cross section is known, π^0 mesons are sampled using rejection sampling from the following distribution:

$$\frac{d\sigma}{d|\vec{p}|d\theta} = \frac{2\pi\sin(\theta)|\vec{p}|^2}{\sqrt{|\vec{p}|^2 + m^2}}\left(E \times \frac{d^3\sigma^{pA_{target}}}{dp^3}\right)_{\pi^0}, \tag{3.18}$$

where $|\vec{p}|$ is the magnitude of the momentum, θ is the polar angle with respect to the beam axis, and m is the π^+ mass. The azimuthal angle φ is then drawn uniformly from $[0, 2\pi]$, fully specifying the relevant kinematics of the generated meson. For more details on the above expression, see Appendix B.

The same formulas are applied when generating other mesons **m** – such as the η meson – using the **BMPT** parametrization in **BdNMC**:

$$\left(\frac{d\sigma}{d|\vec{p}|d\theta}\right)_{\mathbf{m}} = \left(\frac{d\sigma}{d|\vec{p}|d\theta}\right)_{\pi^0}. \tag{3.19}$$

In contrast, **MadDump** handles meson production through externally generated event files, which are parsed to extract the relevant particle kinematics. More details on the implementation used in this work are given in Section 3.2.2.

A final important note: when simulating decays with **MadDump**, the branching ratio $\mathbf{m} \to \gamma A'$ is assumed to be unity. The appropriate correction factor for the results in these channels is thus:

$$2\epsilon^2 \left(1 - \frac{m_{A'}^2}{m_{\mathbf{m}}^2}\right)^3 BR(\mathbf{m} \to \gamma\gamma), \tag{3.20}$$

as seen from Eq. 2.28.

3.1.3 Proton Bremsstrahlung Simulation

The proton bremsstrahlung production channel is fully implemented in **BdNMC**, whereas in **MadDump** it is considered part of the development version of the code. The following section outlines the implementation details of this production channel in both simulation tools.

Form Factors

To improve upon the differential dark photon production rate proposed by Blümlein and Brunner (see Eq. 2.25), **BdNMC** [37] incorporates the enhancement in A' production due to mixing with the ρ and ω meson families. This is done by introducing a timelike electromagnetic form factor $|F_1^p(m_{A'}^2)|^2$ which encodes hadronic structure effects. The form factor used is given by [86]:

$$F_1^p(q^2) = F_1^\rho(q^2) + F_1^\omega(q^2). \tag{3.21}$$

Each contribution is modeled as:

$$F_1^V(q^2) = \sum_{k=V,V',V''} \frac{f_k m_k^2}{g_k(m_k^2 - q^2 - i m_k \Gamma_k)}, \tag{3.22}$$

where $V = \rho$ or ω, and the parameters f_k, g_k, m_k, and Γ_k are fitted to experimental data [86]. It should be noted that this parametrization may have limited validity near resonance peaks, as pointed out by [37].

Including this form factor modifies the expression for the differential A' production rate in Eq. 2.25 to:

$$\frac{d^2N}{dz dp_T^2} = |F_1^p(m_{A'}^2)|^2 w_{pA'}(z, p_T^2) \frac{\sigma_{pp}(s')}{\sigma_{pp}(s)}. \tag{3.23}$$

This formulation is also adopted in **MadDump**.

Table 3.2: Fitted parameters for the proton-proton cross section σ_{pp} as implemented in **BdNMC**.

H_{pp} (mb)	P_{pp} (mb)	$R_{pp,1}$ (mb)	$R_{pp,2}$ (mb)	$\eta_{pp,1}$	$\eta_{pp,2}$	M_{pp} (GeV)
0.2704	34.49	12.98	7.38	0.451	0.549	2.2127

Table 3.3: Fitted parameters for σ_{pp} as used in **MadDump**, following the model in [72].

Z (mb)	B (mb)	$Y1$ (mb)	$Y2$ (mb)	η_1	η_2	s_0 (GeV^2)	s_1 (GeV^2)
35.45	0.308	42.53	33.34	0.458	0.545	5.38[2]	1

Parametrization of σ_{pp}

To evaluate Eq. 3.23, an explicit form for the proton-proton interaction cross section, σ_{pp}, is required. Both **BdNMC** and **MadDump** use parameterizations fitted to experimental data, though the expressions differ between the two implementations.

In **BdNMC**, the parameterization is:

$$\sigma_{pp}(s) = H_{pp}\left[\log(\frac{s}{\bar{s}})\right]^2 + P_{pp} + R_{pp,1}(\frac{s}{\bar{s}})^{-\eta_{pp,1}} - R_{pp,2}(\frac{s}{\bar{s}})^{-\eta_{pp,2}}, \tag{3.24}$$

where $\bar{s} = (2m_p + M_{pp})^2 = 16.72$ GeV^2. The fitted parameter values are listed in Table 3.2.

In **MadDump**, the corresponding parameterization is:

$$\sigma_{pp}(s) = Z + B\left[\log(\frac{s}{s_0})\right]^2 + Y_1(\frac{s}{s_1})^{-\eta_1} - Y_2(\frac{s}{s_1})^{-\eta_2}, \tag{3.25}$$

with parameter values provided in Table 3.3.

Dark Photon Generation

Dark photon generation via proton bremsstrahlung is handled in both **BdNMC** and **MadDump** using sampling techniques based on Eq. 3.23, where p_T and z are uniformly sampled within the user-set bounds. Additionally, the total number of dark photons produced per proton on target is computed by numerically integrating the differential production rate over those same ranges.

As with other production channels in **MadDump**, a correction factor must be applied to the results. In this case, the factor is $\alpha\epsilon^2$, accounting for its omission in the implementation of the $w_{pA'}$ function.

3.2 Simulation Workflow and Postprocessing

This section outlines the complete simulation pipeline, from specifying inputs to performing postprocessing on the generated output.

3.2.1 Setting up Simulations

To perform a **BdNMC** simulation, the primary inputs include the experimental configuration (beam energy, target material and length, detector geometry and composition), the dark sector model parameters ($m_{A'}, m_\chi, \epsilon, \alpha_D$), and the relevant production channels along with their specific input requirements. The experimental setup follows the parameters given in Table 2.1. The chosen model parameters are $\alpha_D = 0.1$, $\epsilon = 10^{-3}$, and $m_{A'} = 3m_\chi$. The dark matter mass m_χ is scanned over a logarithmic grid of approximately 100 points spanning the range $[10^{-3}, 1]$ GeV, with increased resolution near the resonance region around $m_{A'} \approx m_\rho$.

For the production mechanisms, proton bremsstrahlung is employed across the full mass range, using the bounds $z \in [0.1, 0.9]$ and $p_T \in [0, 4]$ GeV, consistent with [29]. The π^0 and η decay channels are included for $m_{A'} < m_{\pi^0}$ and $m_{A'} < m_\eta$ respectively. Both meson channels utilize the **BMPT** distribution, with meson yields set to $6\pi^0$/POT and 0.8η/POT as found in [29] using **Pythia**.

In **MadDump**, the simulation setup requires a **UFO** model file, which defines the relevant interactions, along with detector geometry and material composition. The model parameters, such as masses and couplings, must also be specified. Here, ϵ and α_D are implicitly set via the coupling constants in the interaction terms of the Lagrangian: $\alpha_D = g_D^2/4\pi$ and $\epsilon = g_e/e$, where g_D and g_e denote the couplings of the dark photon to dark matter and electrons, respectively.

The model used was `DM_mesons_2`[3]. The detector configuration matches that listed in Table 2.1, with couplings set to $g_D = 1.121$ and $g_e = 10^{-3} \cdot e$. Mass parameters are consistent with those used in **BdNMC**.

In the proton bremsstrahlung scenario, the beam energy is provided, $E_p = 400$ GeV, along with the bounds $z \in [0.1, 0.9]$ and $p_T^2 \in [0, 16]$ GeV^2. For meson decay channels, a **HepMC** file containing the relevant meson four-momenta is provided. This file is generated externally, and this procedure will be discussed in the following section.

[3]The `DM_mesons_2` UFO model is included in the `example_SHiP` directory distributed with **MadDump**. Additional models are available from the FeynRules model database: `https://feynrules.irmp.ucl.ac.be/wiki/ModelDatabaseMainPage`.

Example input cards for both **BdNMC** and **MadDump** can be found in Listings C.1, C.2, and C.3 in Appendix C.

3.2.2 Pythia

The **HepMC** file used with **MadDump** in this work was generated using **Pythia** version 8.313. To model interactions of the 400 GeV proton beam, a custom ^{96}Mo nucleus "particle" is first defined:

```
pythia.particleData.addParticle(1000420960, "96Mo", 1, 126,
   0, 89.334638710673857);
```

The arguments follow the format: particle ID (in the form 100ZZZAAA0), particle name, spin type: $(2s+1)$, charge type $(3\times\text{charge})$, color type, and the nominal mass m_0 in GeV.

Next, a simulation is configured in which a 400 GeV proton beam collides with stationary ^{96}Mo nuclei. The process is modeled using the *softQCD:Inelastic* flag, consistent with [29]. This enables soft (low-momentum-transfer) inelastic interactions, where the final state contains at least one new particle not present in the initial state, distinguishing it from purely elastic scattering.

These proton-heavy ion collisions are modeled in **Pythia** using the `Angantyr` framework. In this model, the collision is decomposed into multiple parton-level events. These interactions are then hadronized collectively to form the final state. A detailed review of the `Angantyr` model is beyond the scope of this work; readers are referred to the official **Pythia** documentation and to [87] for further details.

Finally, all generated π^0 and η mesons are retained, while other particles are discarded prior to writing the event record to the **HepMC** file. The script used to produce this file is provided in Appendix D.

3.2.3 Simulation Output

For both simulation tools, each run over a given dark matter mass point produces two key outputs: the predicted number of signal events and an event file containing kinematic information – most notably, the momenta of incoming dark matter particles and the outgoing scattered electrons in the detector. This kinematic information is essential for applying selection cuts, as will be discussed in the following section.

3.2.4 Selection Cuts

This section addresses two key questions: why are selection cuts necessary, and how are they applied in practice?

In this study, light dark matter (LDM) particles are detected via their scattering signature $\chi e \to \chi e$ within the SND detector of the SHiP experiment. However, sim-

ilar signatures can also result from background processes involving other particles – in this case, neutrinos. For instance, the interactions $\nu_e e^- \to \nu_e e^-$ or $\nu_e n \to e^- p$ – where the proton escapes detection – can mimic the LDM signal.

To reduce such backgrounds, selection cuts are applied to kinematic properties of the outgoing electron, specifically its energy E_e and its scattering angle θ_e relative to the incoming LDM particle. While neutrino interactions can produce similar final states, the resulting kinematic distributions might differ from those of LDM events. The goal, therefore, is to find a region in the (E_e, θ_e) plane that maximizes signal retention while minimizing the background events.

A detailed analysis of this was performed in [29], which determined that the optimal selection window for LDM scattering in the SHiP experiment is:

$$E_e \in [1, 5] \text{ GeV}, \qquad \theta_e \in [10, 30] \text{ mrad}, \tag{3.26}$$

with an estimated background of 230 events over the full lifetime of the experiment. A dedicated background analysis is beyond the scope of this work, and the selection window and background estimate from [29] are adopted directly. Nonetheless, the E_e - θ_e distributions can be readily extracted from the outputs of both simulation tools and serve as a quick sanity check to verify that the chosen cuts indeed capture a significant fraction of the expected LDM signal events.

To apply the selection cuts in practice, the event file corresponding to each dark matter mass point is parsed to extract the momenta of the incoming LDM particle and the scattered electron for each event. The scattering angle θ_e is computed as the angle between the incoming LDM momentum vector $\vec{p}_\chi$ and the outgoing electron momentum vector $\vec{p}_e$:

$$\theta_e = \arccos\left(\frac{\vec{p}_\chi \cdot \vec{p}_e}{|\vec{p}_\chi||\vec{p}_e|}\right). \tag{3.27}$$

The number of events satisfying the selection criteria defined in Eq. 3.26 is then counted.

It is assumed that the number of generated events per mass point – here 10^4 – is sufficiently large for the fraction of accepted events to be representative of the true distribution. The total predicted number of signal events from the simulation is then scaled by this fraction, yielding the estimated number of signal events expected to pass the selection cuts.

Although this procedure is applied manually to the outputs of both simulation tools, it is worth noting that **BdNMC** includes a built-in feature for applying selection cuts. However, this functionality is intentionally bypassed here to allow for greater transparency and direct control over the analysis.

3.2.5 Signal Evaluation on a Parameter Grid

A common approach to presenting the dark matter detection reach of an experiment is through an exclusion plot in the (m_χ, y) plane, where $y = \epsilon^2 \alpha_D \left(\frac{m_\chi}{m_{A'}}\right)^4$.

In this study, $\alpha_D = 0.1$ is fixed, and the relation $m_{A'} = 3m_\chi$ is imposed throughout. This effectively converts the two-dimensional parameter scan to a grid over (m_χ, ϵ). To achieve high resolution in the final results, this grid needs to be sufficiently dense. The results presented in this work use a grid of 100×500 points, though this is likely more than strictly necessary. Nevertheless, simulating each point in a grid of similar density would be overly expensive in terms of computational resources.

Fortunately, this burden can be significantly reduced by exploiting key scaling behavior: when dark photon decay is dominated by $A' \to \chi\bar{\chi}$ – ensured by the conditions $2m_\chi < m_{A'}$ and $\alpha_D \gg \alpha\epsilon^2$ – the number of signal events scales as $\alpha_D \epsilon^4$ for a fixed mass point.

Under these conditions, it is enough to simulate each m_χ value for a single reference coupling ϵ_0, and then analytically rescale the results to obtain predictions for other ϵ values, also satisfying the same assumptions.

This significantly reduces the computational overhead, as simulations are only required along the m_χ axis. The full procedure is outlined in Algorithm 1.

Algorithm 1 Generate signal predictions over a grid of (m_χ, ϵ)

Define mass range: $m_\chi \in [m_\chi^{\min}, m_\chi^{\max}]$
Fix α_D
Select a range: $\epsilon \in [\epsilon^{\min}, \epsilon^{\max}]$ such that $\alpha_D \gg \epsilon^2\alpha$
Choose a reference value: $\epsilon_0 \in [\epsilon^{\min}, \epsilon^{\max}]$
for each m_χ in $[m_\chi^{\min}, m_\chi^{\max}]$ **do**
    Set $m_{A'} \leftarrow 3m_\chi$
    Run simulation: $\text{Events}(m_\chi, \epsilon_0) \leftarrow \text{Simulate}(m_\chi, m_{A'}, \epsilon_0, \alpha_D)$
    for each $\epsilon \in [\epsilon^{\min}, \epsilon^{\max}]$ **do**
        Scale result: $\text{Events}(m_\chi, \epsilon) \leftarrow \left(\frac{\epsilon}{\epsilon_0}\right)^4 \cdot \text{Events}(m_\chi, \epsilon_0)$
    end for
end for

3.2.6 Statistics for Exclusion Plots

Even when an experiment does not observe a signal – meaning the number of observed events N_{obs} is consistent with the expected background b – useful information can still be extracted. In particular, models predicting a large number of signal events can be constrained or ruled out at some confidence level if the observed number of events remains consistent with the background expectation.

To quantify this, an upper bound s_{up} on the predicted number of signal events that would still be compatible with the observed result, given a specified confidence level $1 - \alpha$, is computed. Any model predicting a number of signal events $s \geq s_{up}$ is then excluded at confidence level $1 - \alpha$, assuming no significant excess of events is observed in the experiment.

In this statistical framework, the total number of observed events $N_{obs} = b + s$ is modeled as a Poisson-distributed random variable, appropriate for event-counting experiments such as this:

$$N_{obs} \sim \text{Poisson}(\lambda = b + s). \tag{3.28}$$

Under the null hypothesis, the expected number of events is $\lambda = b$ (the SM prediction is $s = 0$), with the standard deviation $\sqrt{\lambda} = \sqrt{b}$. Next, the Poisson distribution is approximated by a normal distribution – in line with [78] for example – yielding a somewhat conservative upper limit.

Using a one-sided interval under the normal approximation, the exclusion condition can be expressed in terms of the z-score:

$$z_\alpha \geq \frac{N_{obs} - \lambda}{\sqrt{\lambda}} = \frac{(b + s) - b}{\sqrt{b}} = \frac{s}{\sqrt{b}}. \tag{3.29}$$

Solving for s:

$$s \leq z_\alpha \sqrt{b} = s_{up}. \tag{3.30}$$

Here, a confidence level of 90% (in line with [29]) is used, corresponding to the one-sided z-score of $z_{0.1} \approx 1.28$. With an expected background of $b = 230$ events, the upper limit becomes:

$$s \leq 1.28 \cdot \sqrt{230} \approx 19.4. \tag{3.31}$$

This means that if the observed number of events in the real SHiP experiment is consistent with the background ($N_{obs} \approx b = 230$), then any combination of model parameter values $(m_{A'}, m_\chi, \epsilon, \alpha_D)$ predicting more than ~ 19.4 signal events can be excluded at the 90% confidence level.

3.3 Extending UFO to Majorana Fermions

The `DM_mesons_2` **UFO** model used here includes both complex scalar and Dirac fermion dark matter candidates, denoted by `Xc` and `Xd`, respectively. The dark photon mediator is referred to as `Y1`, indicating its spin-1 nature.

To incorporate a Majorana fermion dark matter candidate, labeled `Xm`, the existing **UFO** model must be extended. Although this could be achieved through a full implementation in **FeynRules**, a more direct approach was chosen: manual insertion of the necessary definitions directly into the relevant **UFO** files. This extension involves modifications to four key files in the `DM_mesons_2` directory: `parameters.py`,

`particles.py`, `vertices.py`, and `couplings.py`.

In `parameters.py`, the mass of the new Majorana particle is introduced with the following addition:

```
MXm = Parameter(name = 'MXm',
                nature = 'external',
                type = 'real',
                value = 10.,
                texname = '\\text{MXm}',
                lhablock = 'MASS',
                lhacode = [ 5000522 ])
```

The value of 10 GeV is arbitrary at this stage and can be modified in the simulation input cards as needed.

Next, in `particles.py`, the Majorana fermion `Xm` is added:

```
Xm = Particle(pdg_code = 5000522,
              name = 'Xm',
              antiname = 'Xm',
              spin = 2,
              color = 1,
              mass = Param.MXm,
              width = Param.ZERO,
              texname = 'Xm',
              antitexname = 'Xm',
              charge = 0,
              GhostNumber = 0,
              LeptonNumber = 0,
              Y = 0)
```

Notably, the particle is its own antiparticle (`antiname = 'Xm`), satisfying the Majorana condition. Its spin value of 2 corresponds to spin-1/2 ($2s + 1 = 2$), and it is color neutral ($2c + 1 = 1$).

In `vertices.py`, a tree-level vertex involving two `Xm` partiles and the dark photon `Y1` is added:

```
V_170 = Vertex(name = 'V_170',
               particles = [ P.Xm, P.Xm, P.Y1 ],
               color = [ '1' ],
               lorentz = [ L.FFV2 ],
               couplings = {(0,0):C.GC_111})
```

Here, the vertex name is arbitrary and is needed simply to avoid conflict with existing entries. The `color` assignment indicates a color-neutral interaction, and `L.FFV2` specifies an axial-vector coupling for a fermion-fermion-vector Lorentz structure, defined in `lorentz.py`.

Finally, the coupling used in this vertex is defined in `couplings.py`:

```
GC_111 = Coupling(name = 'GC_111',
                  value = '(complex(0,1)*gAXm)/2',
                  order = {'DMV':1})
```

The exact coupling name is not physically significant. The expression corresponds to the axial-vector coupling $g_D^A/2$ in Eq. 2.16, and the interaction is marked as part of the dark matter sector via the `DMV` order tag.

4

Results

This chapter presents the results and key findings derived from the methodologies and models discussed in the preceding chapters. It includes a comparison between the two simulation tools, **BdNMC** and **MadDump**, as well as an evaluation of the SHiP experiment's sensitivity to the Majorana and Dirac fermion dark matter candidates.

4.1 Comparison of BdNMC and MadDump

From the introduction of the two frameworks, it can be seen that the scope and flexibility of **MadDump** is wider. It can accommodate other settings than proton beams, dark sector models besides complex scalar dark matter, and detection via decays in addition to scattering. Though in the setting of the SHiP experiment as considered in this thesis – where light dark matter is produced in a proton beam dump and detected via scattering – most of these flexibility aspects are not needed or utilized, but are nonetheless noteworthy for the comparison.

4.1.1 Proton Bremsstrahlung Channel

The stated formulas for proton bremsstrahlung in both tools are structurally very similar. The primary difference lies in the parameterizations of the proton-proton cross section. However, this difference is minor within the energy range $s \in [0.3, 10^4]$, as shown in Figure 4.1. The figure also indicates the relevant center-of-mass energy squared for the SHiP experiment, $s = 2m_p E_p$. In the simulations for this work, typical dark photon energies are of the scale $E_{A'} \sim 10^1 - 10^2$ GeV, implying $s' = 2m_p(E_p - E_{A'})$ remains well within the region where the two parameterizations yield similar results.

The more significant discrepancy arises from the implementation in **BdNMC**, which does not quite reflect some of the stated formulas. Two specific issues are identified:

- The splitting function in the code reads:

$$w_{pA'}(z, p_T^2, m_{A'}) = \frac{\epsilon^2 \alpha}{\textcircled{4} \cdot (2\pi H)} \left\{ \frac{1 + (1-z)^2}{z} - 2z(1-z) \left[\frac{2m_p^2 + m_{A'}^2}{H} \right. \right. \quad (4.1)$$

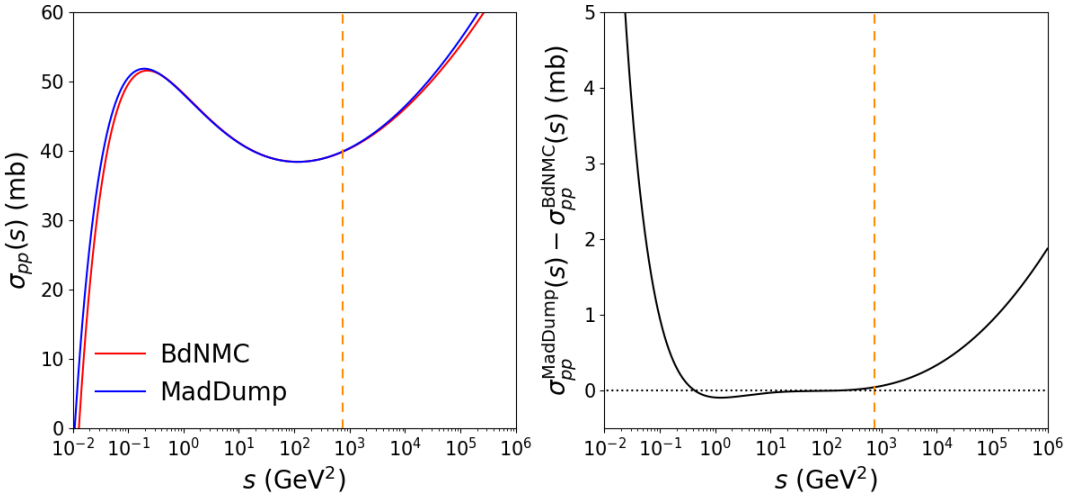

Figure 4.1: The left panel shows the proton-proton interaction cross section σ_{pp} as a function of the center-of-mass energy squared s. Results are presented for the parameterization used in both **BdNMC** (red) and **MadDump** (blue). The right panel shows the difference $\sigma_{pp}^{\textbf{MadDump}} - \sigma_{pp}^{\textbf{BdNMC}}$ as a function of s, with the horizontal dotted black line indicating zero for reference. In both panels, the vertical dashed orange line marks the relevant center-of-mass energy squared for the SHiP experiment, given by $s = 2m_p E_p$.

$$-2\left(\frac{z \cdot m_p^2}{H}\right)^2\Bigg] + 2z(1-z)\Big[\textcircled{z} + (1-z)^2\Big]\left(\frac{m_p m_{A'}}{H}\right)^2 + 2z\left(\frac{(1-z)m_{A'}^2}{H}\right)^2\Bigg\},$$

where two inconsistencies are highlighted (circled in the equation): an extraneous factor of 4 in the denominator, and a substitution of z where the correct term should be 1.

- The computation of the dark photon yield per proton on target,

$$N = \int_{z_{min}}^{z_{max}} \int_{p_{T,min}}^{p_{T,max}} \frac{d^2N}{dz dp_T^2} dz dp_T^2, \tag{4.2}$$

is performed over the interval $[p_{T,\text{min}}, p_{T,\text{max}}]$ instead of the proper squared limits $[p_{T,\text{min}}^2, p_{T,\text{max}}^2]$. A similar issue is found in the evaluation of the differential distribution $\frac{d^2N}{dz dp_T^2}$ during dark photon momentum sampling.

The cumulative effect of the above points is demonstrated in Figure 4.2, which compares simulation results from the original **BdNMC** and a modified version incorporating the above fixes. Also shown are the results from **MadDump**, which exhibit good agreement with the modified **BdNMC** output.

4.1.2 π^0 and η Meson Decay Channels

As in the case of proton bremsstrahlung, a few issues were identified in the implementation of the **BMPT** parametrization for meson production in **BdNMC**. These

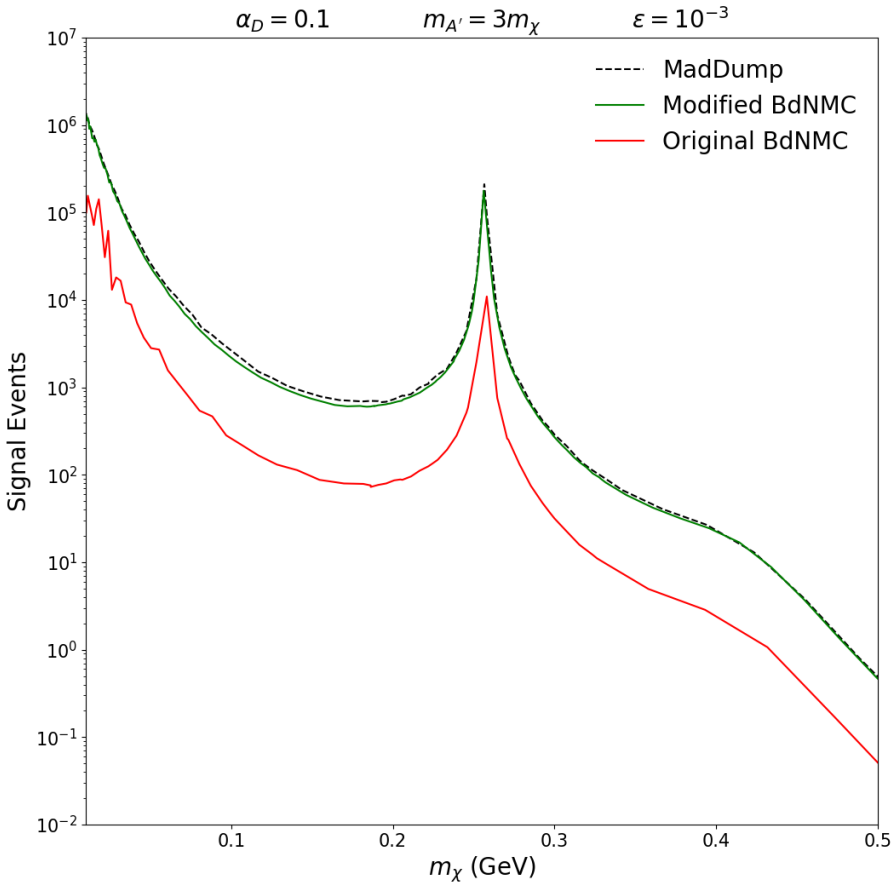

Figure 4.2: Estimated number of signal events as a function of the dark matter mass m_χ for the proton bremsstrahlung production channel in the complex scalar dark matter model. Results are shown for three cases: the original **BdNMC** implementation (solid red), the modified **BdNMC** version with corrections described in the text (solid green), and **MadDump** (dashed black).

issues, though subtle, are worth noting for completeness.

Firstly, the rescaling of the meson production distribution from beryllium (the material for which the **BMPT** parameterization was originally fitted) to the desired target material relies on the atomic mass number of beryllium, denoted A_{Be}. In the source code, this value was set to 8. However, nearly 100% of terrestrial beryllium is composed of the isotope ^{9}Be [88], and the value should therefore be $A_{Be} = 9$.

Second, similar to the discrepancy found in the proton bremsstrahlung implementation, the variable p_T was used in place of p_T^2 in the expression of $\alpha(x_F)$ (as defined in Eq. 3.17). Both of these issues are minor in terms of their numerical impact, note however that all meson decay results shown for **BdNMC** in this thesis are based on a revised version of the code.

A significant difference in meson decay simulation between **BdNMC** and **MadDump** arises from the underlying meson generation method: **BdNMC** uses the analytical **BMPT** parameterization, while **MadDump** utilizes event data generated by **Pythia**.

Figure 4.3 compares the resulting distributions from both methods for both π^0 and η mesons. The **BMPT**-based samples were generated via rejection sampling using 2000 burn-in samples and 10000 final samples, while the **Pythia**-based distributions were obtained from the full simulated data set of 10000 events. Subfigures 4.3a and 4.3b show the results for π^0 and η mesons, respectively.

The transverse momentum components (p_x, p_y) are in good agreement between the two methods for the π^0 mesons, although the **Pythia**-based distribution is slightly wider, indicating a marginally larger angular spread. This effect is more pronounced for η mesons.

In contrast, differences in the energy E and longitudinal momentum p_z distributions are more noticeable. For both π^0 and η mesons, the **Pythia** samples appear softer – the spectrum is shifted towards lower energies – compared to those generated using the **BMPT** parameterization.

Figure 4.4 presents the estimated number of signal events for the two meson decay channels, as computed using both **BdNMC** and **MadDump**. While the overall trends are similar, a consistent offset is observed: **BdNMC** predicts a higher number of signal events compared to **MadDump**.

4.1.3 Combined Production Channels

The results from both **BdNMC** and **MadDump** simulations for the three production channels have been converted into an exclusion plot, shown in Figure 4.5. As observed previously, **BdNMC** predicts higher sensitivity in the mass regions dominated by π^0 and η decays. In contrast, the sensitivity estimates from both tools

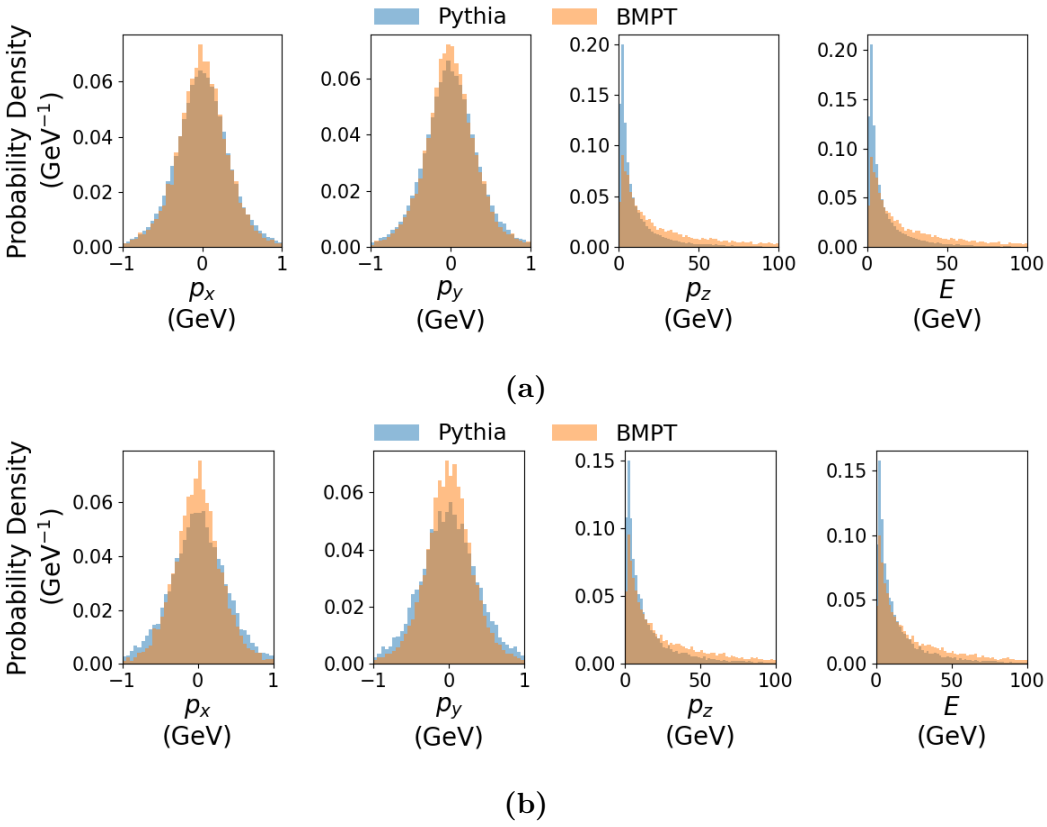

(a)

(b)

Figure 4.3: Probability density (normalized counts per bin) for the momentum components p_x, p_y, p_z and total energy E of sampled particles. The samples are drawn from two sources: **Pythia** simulations (blue) and the parametrized **BMPT** distribution (orange). Results are shown for two meson types: (a) π^0, (b) η.

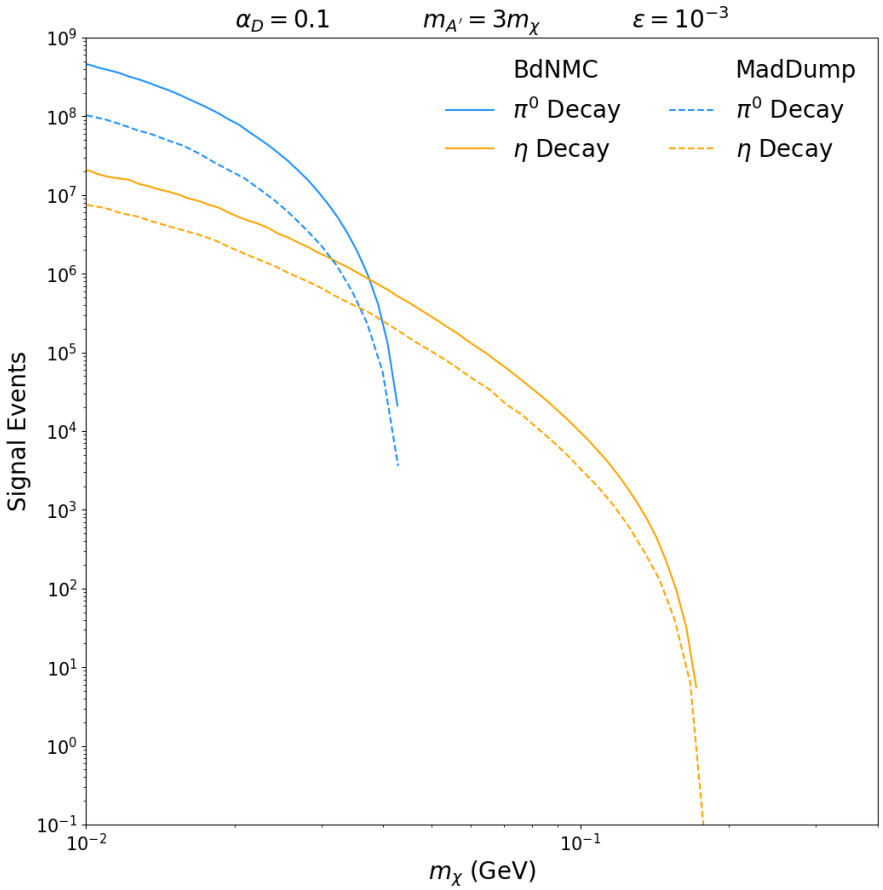

Figure 4.4: Estimated number of signal events as a function of the dark matter mass m_χ for the π^0 (blue) and η (orange) meson decay channels in the complex scalar dark matter model. Results are shown from both **BdNMC** (solid lines) and **MadDump** (dashed lines).

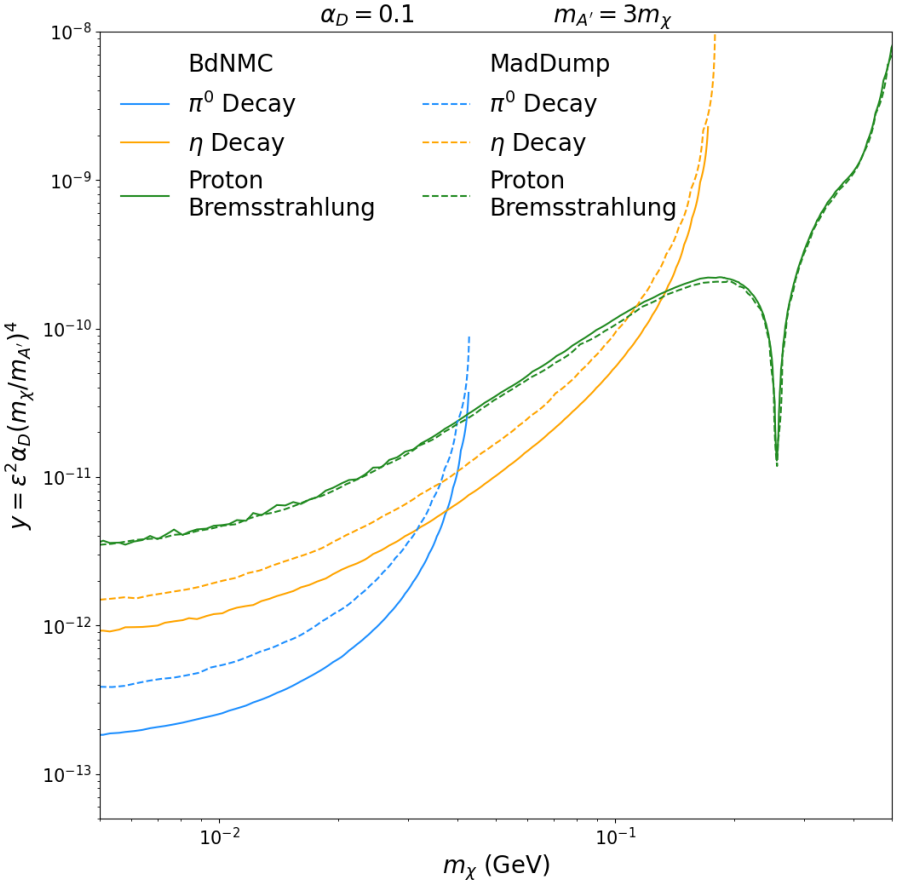

Figure 4.5: Exclusion plot at 90% confidence level, showing the individual contributions from each production channel: π^0 decay (orange), η decay (blue), and proton bremsstrahlung (green). Results are shown for both **BdNMC** (solid lines) and **MadDump** (dashed lines).

agree well in the region where proton bremsstrahlung is the dominant production mechanism.

Figure 4.6 presents the exclusion plot combining all three production channels into a total sensitivity estimate for both **BdNMC** and **MadDump**. For comparison, the exclusion limit obtained from similar simulations in [29] is shown in blue. The figure also includes current experimental constraints from BaBar (orange shaded region) and NA64 (green shaded region), as well as the thermal relic target for a complex scalar dark matter model, providing context for the parameter space coverage [56].

In the lower mass range, where π^0 and η decays dominate, the **MadDump** results closely match the reference, while **BdNMC** gives a higher sensitivity estimate.

In the region dominated by proton bremsstrahlung, both **BdNMC** and **MadDump**

yield consistent sensitivity estimates, which are slightly larger than the sensitivity estimate in the reference.

4.2 Comparison Across Dark Matter Models

Figure 4.7 presents the exclusion plot combining all three production channels to provide total sensitivity estimates for the complex scalar, Majorana fermion, and Dirac fermion dark matter models, as obtained using **MadDump**. Also shown are current experimental constraints from BaBar (orange shaded region) and NA64 (green shaded region), along with the thermal relic targets for the complex scalar, Majorana fermion, and pseudo-Dirac fermion dark matter models, providing context for the parameter space coverage [56].

Across the entire mass range considered, the Dirac fermion and the complex scalar models produce nearly identical sensitivity curves. In contrast, the Majorana fermion model consistently predicts a lower sensitivity, offset by a roughly constant factor throughout the range.

4.3 Kinematic Distributions of Scattered Electrons

Figure 4.8 presents the distributions of electrons scattered off dark matter in the SHiP detector, organized by production channel (columns) and dark matter model or simulation tool (rows). The models considered are the complex scalar (CS), Majorana fermion (MF), and Dirac fermion (DF). The CS model was simulated using both **BdNMC** and **MadDump**, while the MF and DF models were simulated only with **MadDump**.

Key observations from the figure include:

- A clear correlation is observed: increasing the mass of the dark matter (and the dark photon) results in higher electron energies and smaller scattering angles.

- All three dark matter models yield very similar kinematic distributions for each production channel.

- The CS model simulated with **BdNMC** consistently shows a narrower angular spread at each given energy compared to the **MadDump** simulation, across all three production channels.

- The selection window – defined as $E_e \in [1, 5]$ GeV and $\theta_e \in [10, 30]$ mrad – captures a significant fraction of events for the lower mass benchmarks (20 MeV and 60 MeV). However, for the 200 MeV case, the broader spread of the distributions leads to fewer events falling within the selection window.

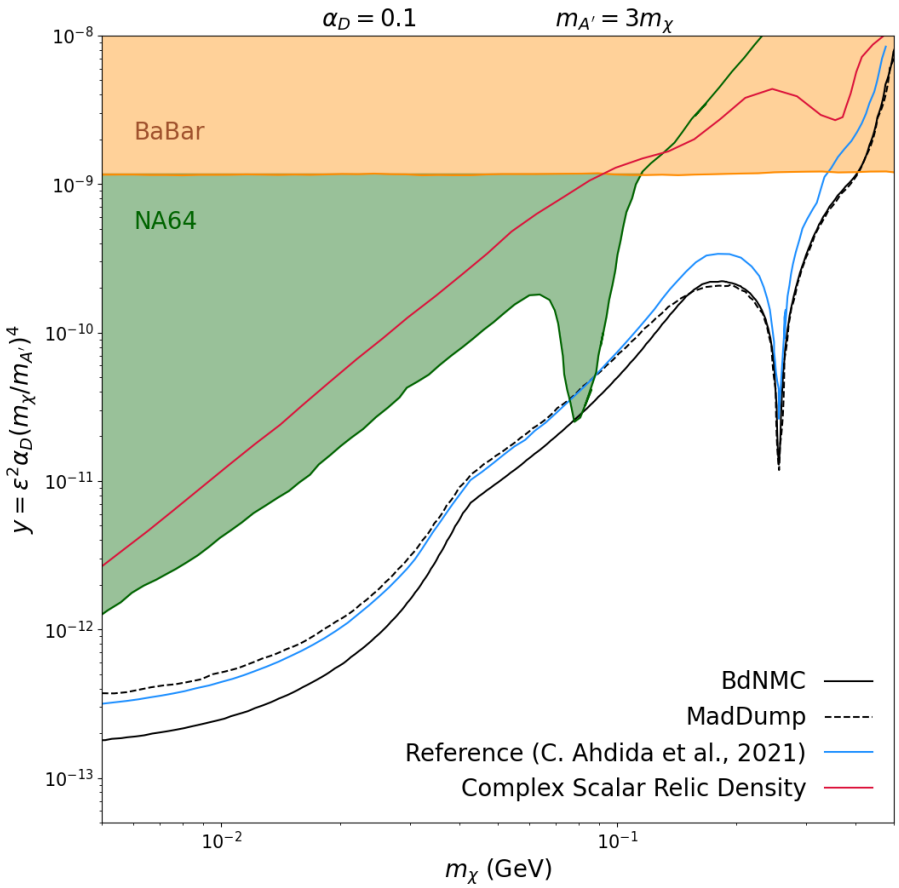

Figure 4.6: Exclusion plot at 90% confidence level, combining contributions from all three production channels: π^0 and η decay, and proton bremsstrahlung. Results are shown for both **BdNMC** (solid black) and **MadDump** (dashed black). For comparison, the exclusion limit obtained from similar simulations in [29] is shown as a solid blue line. Existing experimental constraints from BaBar (orange shaded region) and NA64 (green shaded region) are also displayed, along with the thermal relic target for the complex scalar dark matter model (solid red), obtained from [56].

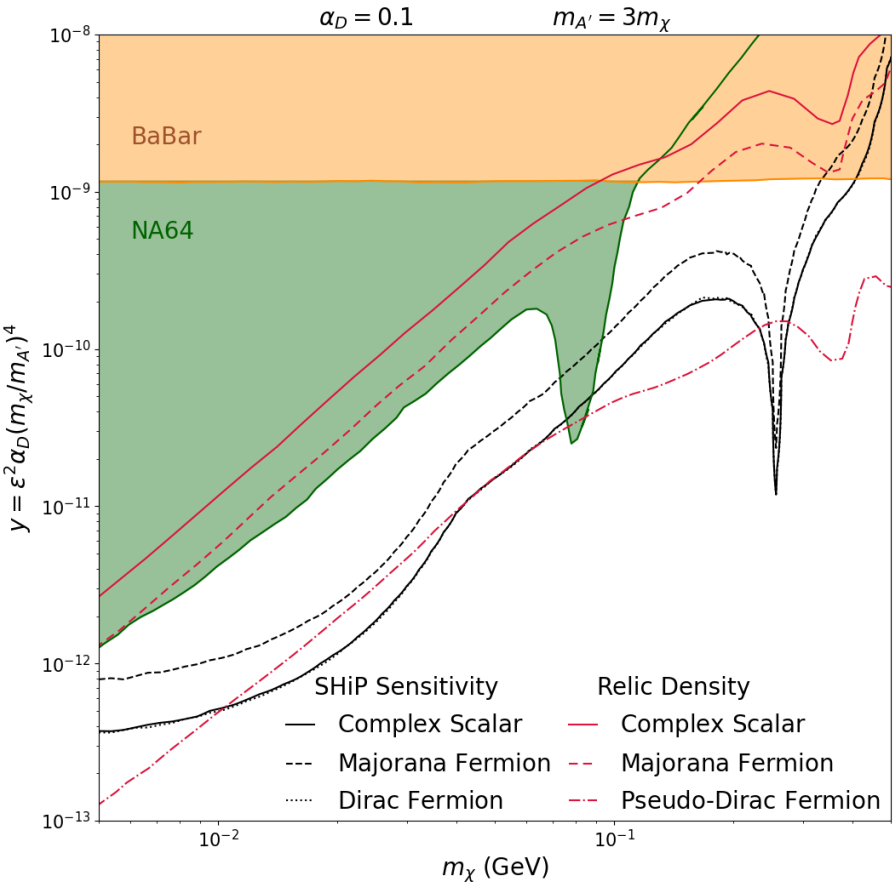

Figure 4.7: Exclusion plot at 90% confidence level, combining contributions from all three production channels: π^0 and η decay, and proton bremsstrahlung. Shown are the results obtained using **MadDump** for each dark matter candidate: complex scalar (solid black), Majorana fermion (dashed black), and Dirac fermion (dotted black). Also included are current experimental constraints from BaBar (orange shaded region) and NA64 (green shaded region), along with the thermal relic targets for complex scalar (solid red), Majorana fermion (dashed red), and pseudo-Dirac fermion (dash-dotted red) dark matter models, obtained from [56].

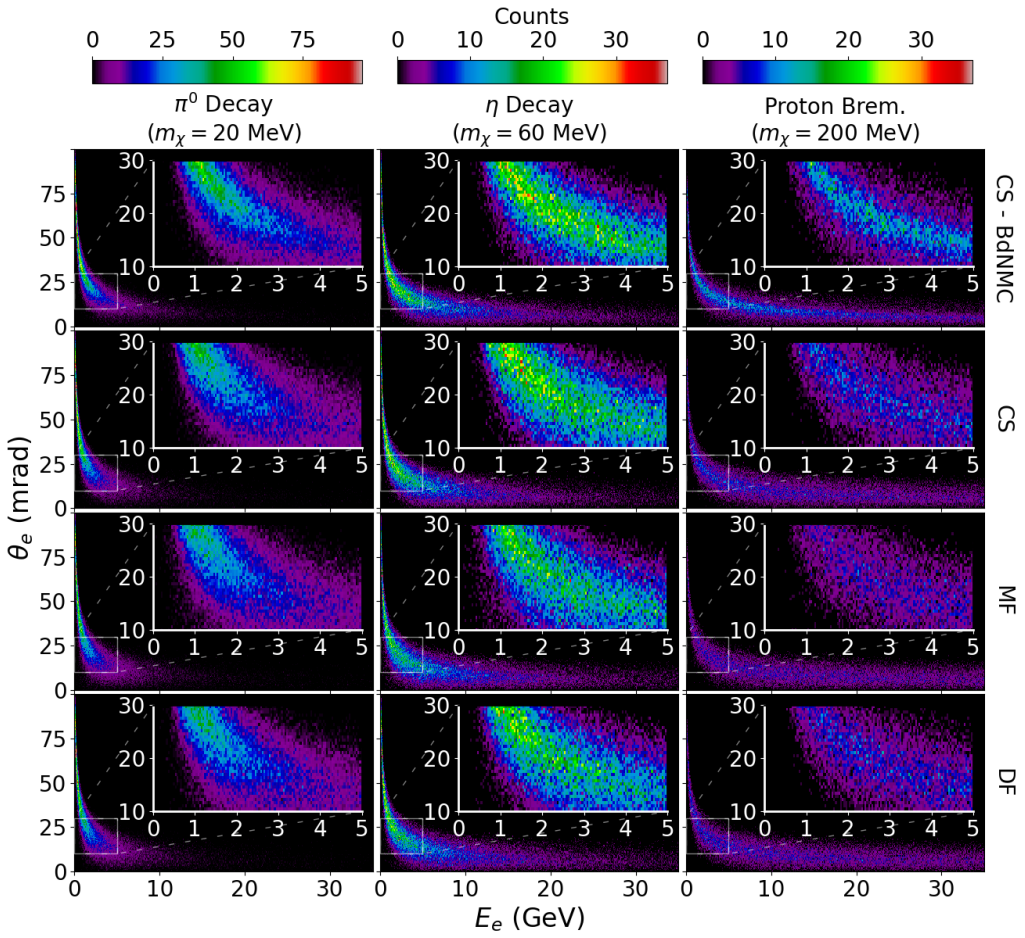

Figure 4.8: Distributions of simulated scattered electrons in the (E_e, θ_e) plane, where E_e is the electron energy and θ_e the scattering angle, using the baseline parameters: $\alpha_D = 0.1$, $\epsilon = 10^{-3}$, and $m_{A'} = 3m_\chi$. Each row corresponds to one of the dark matter models: complex scalar (CS), Majorana fermion (MF), and Dirac fermion (DF). The CS model was simulated using both **BdNMC** and **MadDump**, while the MF and DF models were simulated using only **MadDump**. Each column represents one of the three production channels: π^0 decay, η decay, and proton bremsstrahlung, simulated with $m_\chi = 20$ MeV, 60 MeV, and 200 MeV, respectively. Each plot includes a zoomed-in inset highlighting the selection cut window: $E_e \in [1, 5]$ GeV and $\theta_e \in [10, 30]$ mrad.

5
Discussion

The discrepancies identified in the proton bremsstrahlung implementation of **BdNMC** had a noticable impact on the sensitivity estimates. Fortunately, these issues were relatively straightforward to amend. After the corrections, the results showed good agreement with those obtained using **MadDump**.

Both tools incorporate the widely used modified Weizsäcker-Williams approximation proposed by Blümlein and Brunner [72] in their proton bremsstrahlung modeling. However, this approach has faced criticism in other studies [73, 75, 89], where it is seen to consistently estimate a higher differential cross section compared to other models. Given the implications for sensitivity estimates, the validity of this approximation should be scrutinized further. If confirmed to overestimate the cross section, a different approach may be necessary in both tools to ensure accurate modeling.

Minor issues were found in the **BMPT** distribution implementation in **BdNMC**, though these were easily corrected and had only a negligible impact on results. A significant difference between the two simulation tools arises from the choice of meson generation strategy. The broader angular spread observed in the **Pythia**-based meson distributions, shown in Figure 4.3, likely results in a wider spread of the produced dark matter particles. This would reduce the fraction of particles that intersect with the detector, and may shorten the effective path length through the detector volume for those that do, ultimately decreasing the expected number of scattering events.

This broader angular distribution may also lead to a wider spread in the angles of scattered electrons, as seen in the energy-angle distributions for the complex scalar model in Figure 4.8. Since the electron energy distributions are quite similar between **BdNMC** and **MadDump**, the angular differences contribute to a slightly reduced acceptance in **MadDump**, with fewer events passing the selection cuts.

Hence, the observed difference in the estimations between **BdNMC** and **MadDump** in the two meson decay channels, as seen in Figure 4.4, is primarily attributed to the different meson generation methods. This sensitivity to the generation method was also noted in [90].

Another notable aspect of **BdNMC** is the use of the charged pion mass in the **BMPT** differential cross section formula, which is used to generate any of the considered meson types. Since the original **BMPT** fit was developed for π^+ and π^-,

applying it to other mesons without adjustment could be problematic – especially for heavier ones such as the ω meson. The validity of this approach could be an interesting topic of future work.

Turning to the exclusion plots, the SHiP experiment is expected to significantly improve upon the limits set by NA64 and BaBar in the considered mass range. While the shown thermal target lines for the complex scalar and Majorana fermion models may already be probed by these experiments, the SHiP experiment remains highly relevant. For instance, increasing α_D would shift the thermal target lines downward relative to the exclusion lines. Additionally, other thermal dark matter models – such as the pseudo-Dirac fermion – might not be probed by current experiments but could fall within SHiP's sensitivity range. It is also important to note that thermal freeze-out is just one of many possible mechanisms for dark matter production in the early universe, explaining the observed relic abundance.

In the regions where meson decay dominates, the **MadDump** results align well with those from [29], whereas **BdNMC** results deviate. Interestingly, in the proton bremsstrahlung-dominated regime, this trend reverses: **MadDump** and **BdNMC** agree with each other, but not with [29]. The source of this discrepancy remains unclear, although discussions with one author of the mentioned paper are ongoing.

As shown in Figure 4.7, SHiP's sensitivity to the complex scalar and Dirac fermion models are nearly identical, while the Majorana fermion model shows a consistent offset by roughly a constant factor. The energy-angle distributions across the three models (Figure 4.8) appear very alike. This similarity between the models is likely due to the model differences only manifesting in the third step of the simulation chain: the dark matter-electron scattering. The dark photon production is independent of the dark matter candidate type, and its branching ratio to dark matter is approximately one across all three models. Therefore, the only opportunity for model-specific behavior lies in the scattering process, which could explain the exhibited similarities.

Regarding the selection cuts, the chosen acceptance window appears to be well-suited for the low and intermediate dark matter masses (and thus the dark photon mass due to $m_{A'} = 3m_\chi$). At higher masses, the broader energy distribution, as seen in Figure 4.8, makes it more challenging to define a compact window that captures a substantial number of signal events. Still, a definitive statement on the effectiveness of the selection cannot be made without a corresponding background study – as the purpose of selection cuts is to optimize the signal-to-background ratio – which was not performed here.

In summary, **MadDump**, built on the **MadGraph5_aMC@NLO** framework, provides a high degree of robustness, flexibility, and control in terms of model implementation, production channels, and detection mechanisms. **BdNMC**, on the other hand, has more emphasis on simplicity and ease of use, making it more accessible and well-suited for studies where detailed simulation control is less essential.

6
Conclusion & Outlook

During the course of this work, a few implementation-level inconsistencies were identified in **BdNMC**, some of which had a sizable impact on the resulting sensitivity estimates. Beyond these, the primary source of variation between the two simulation tools arose in the meson decay production channels. These differences stem largely from the distinct approaches each tool uses to generate meson kinematics, leading to different transverse momentum and energy distributions. Consequently, **BdNMC** tended to produce higher sensitivity estimates for the SHiP experiment compared to **MadDump** in the meson decay-dominated regions.

When comparing the results obtained in this work to those published by the SHiP collaboration [29], it was found that **MadDump** showed strong agreement in the regions where the meson decays dominate, with some deviation emerging in the proton bremsstrahlung-dominated regime. The origin of this discrepancy remains unclear, and discussions with one of the authors of the SHiP study are ongoing. In contrast, **BdNMC** showed higher sensitivity estimates compared to the SHiP collaboration's results in both the proton bremsstrahlung and meson decay regions.

The sensitivity projections for the SHiP experiment to Majorana and Dirac fermion dark matter candidates show a significant improvement in parameter space coverage compared to existing limits. These findings further underscore the SHiP experiment's potential in probing new regions of light dark matter scenarios.

In terms of simulation frameworks, **MadDump** provides a high degree of robustness, flexibility, and control over simulation settings and models. **BdNMC**, though less flexible, instead has the advantage of simplicity and user-friendliness.

Building on this study, several interesting directions for future work include:

- Re-evaluating the modified Weizsäcker-Williams approximation proposed by Blümlein and Brunner, which underpins the proton bremsstrahlung calculations in both **BdNMC** and **MadDump**. Since this approximation is widely used, assessing its validity is important beyond the scope of this work.

- Investigating the validity of the **BMPT** $\pi^{\pm}$ distribution for mesons beyond its original scope, specifically for π^0 and η mesons.

- Extending the comparison between the simulation tools to other experiments

featuring different production channels and detection mechanisms, which may reveal further discrepancies or limitations in either of the simulation tools not captured here.

- Exploring additional dark matter models, such as pseudo-Dirac fermions, or models with scalar mediators to evaluate the sensitivity of the SHiP experiment further.

These avenues, alongside the many open questions in the broader field of dark matter research, represent valuable opportunities for future investigation.

Bibliography

[1] F. W. Bessel, "Extract from the translation of a letter from Professor Bessel, dated Konigsberg, 10th of August, 1844: On the variations of the proper motions of Procyon and Sirius," *MNRAS*, vol. 6, no. 11, pp. 136–141, Dec. 1844, doi: https://doi.org/10.1093/mnras/6.11.136a

[2] B. Kelvin. (1904), Baltimore lectures on molecular dynamics and the wave theory of light [Online]. Available: https://archive.org/details/baltimorelecture00kelviala]

[3] F. Zwicky, "Republication of: The redshift of extragalactic nebulae," *Gen. Relativ. Gravit.*, vol. 41, pp. 207–224, Jan. 2009, doi: https://doi.org/10.1007/s10714-008-0707-4

[4] N. Aghanim et al. (Planck Collaboration), "Planck 2018 results - VI. Cosmological parameters," *Astron. Astrophys.,* vol. 641, Sep. 2020, Art. no. A6, doi: https://doi.org/10.1051/0004-6361/201833910

[5] G. Bertone, and D. Hooper, "History of dark matter," *Rev. Mod. Phys.,* vol. 90, no. 4, p. 045002, Oct. 2018, doi: https://doi.org/10.1103/RevModPhys.90.045002

[6] M. Battaglieri et al., "US Cosmic Visions: New Ideas in Dark Matter 2017: Community Report," Jul. 2017, *arXiv:*1707.04591, doi: https://doi.org/10.48550/arXiv.1707.04591

[7] A. Einstein, "Die Grundlage der allgemeinen Relativitätstheorie," *Ann. Phys.,* vol. 353, no. 7, pp. 769-822, Mar. 1916, doi: https://doi.org/10.1002/andp.19163540702

[8] F. Zwicky, "On the Masses of Nebulae and of Clusters of Nebulae," *ApJ,* vol. 86, no. 3, pp. 217-246, Oct. 1937, doi: https://ui.adsabs.harvard.edu/link_gateway/1937ApJ....86..217Z/doi:10.1086/143864

[9] R. Massey, T. Kitching, and J. Richard, "The dark matter of gravitational lensing", *Rep. Prog. Phys.,* vol. 73, no. 8, p. 086901, Jul. 2010, doi: https://doi.org/10.1088/0034-4885/73/8/086901

[10] G. Bertone, D. Hooper, and J. Silk, "Particle dark matter: evidence, candidates and constraints," *Phys. Rep.,* vol. 405, no. 5-6, pp. 279-390, Jan. 2005, doi: https://doi.org/10.1016/j.physrep.2004.08.031

[11] K. G. Begeman, A. H. Broeils, and R. H. Sanders, "Extended rotation curves of spiral galaxies : dark haloes and modified dynamics," *Mon. Not. R. Astron. Soc.,* vol. 249, no. 3, pp. 523-537, Apr. 1991, doi: https://doi.org/10.1093/mnras/249.3.523

[12] D. Clowe et al., "A Direct Empirical Proof of the Existence of Dark Matter," *ApJ,* vol. 648, no. 2, p. L109, Aug. 2006, doi: https://dx.doi.org/10.1086/508162

[13] X-ray: NASA/CXC/CfA/M.Markevitch et al.;
Optical: NASA/STScI; Magellan/U.Arizona/D.Clowe et al.;
Lensing Map: NASA/STScI; ESO WFI; Magellan/U.Arizona/D.Clowe et al.
Release date: Aug. 2006
Available: https://chandra.harvard.edu/press/06_releases/press_082106.html

[14] W. Hu, and S. Dodelson, "Cosmic Microwave Background Anisotropies," *Annu. Rev. Astron. and Astrophys.,* vol. 40, pp. 171-216, Sep. 2002, doi: https://doi.org/10.1146/annurev.astro.40.060401.093926

[15] M. Bauer, and T. Plehn, *Yet Another Introduction to Dark Matter: The Particle Physics Approach,* Lecture Notes in Physics, Cham, Switzerland: Springer, 2019, doi: https://doi.org/10.1007/978-3-030-16234-4

[16] M. Milgrom, "A modification of the Newtonian dynamics as a possible alternative to the hidden mass hypothesis," *ApJ,* vol. 270, pp. 365-370, Jul. 1983, doi: https://ui.adsabs.harvard.edu/link_gateway/1983ApJ...270..365M/doi:10.1086/161130

[17] J. D. Bekenstein, "Relativistic gravitation theory for the modified Newtonian dynamics paradigm," *Phys. Rev. D,* vol. 70, no. 8, p. 083509, Oct. 2004, doi: https://doi.org/10.1103/PhysRevD.70.083509

[18] L. J. Hall, K. Jedamzik, J. March-Russell, and S. M. West, "Freeze-In Production of FIMP Dark Matter," *J. High Energy Phys.,* vol. 2010, Mar. 2010, Art. no. 80, doi: https://doi.org/10.1007/JHEP03(2010)080

[19] G. Jungman, M. Kamionkowski, and K. Griest, "Supersymmetric dark matter," *Phys. Rep.,* vol. 267, no. 5-6, pp. 195-373, Mar. 1996, doi: https://doi.org/10.1016/0370-1573(95)00058-5

[20] T. Zimmermann, J. Alvey, D. Marsh, M. Fairbairn, and J. I. Read, "Dwarf Galaxies Imply Dark Matter Is Heavier than 2.2×10^{-21} eV," *Phys. Rev. Lett.,* vol. 134, no. 15, p. 151001, Apr. 2025, doi: https://doi.org/10.1103/PhysRevLett.134.151001

[21] E. G. M. Ferreira, "Ultra-light dark matter," *Astron. Astrophys. Rev.,* vol. 29, Sep. 2021, Art. no. 7, doi: https://doi.org/10.1007/s00159-021-00135-6

[22] E. W. Kolb, and A. J. Long, "Superheavy dark matter through Higgs portal operators," *Phys. Rev. D,* vol. 96, no. 10, p. 103540, Nov. 2017, doi: https://doi.org/10.1103/PhysRevD.96.103540

[23] E. W. Kolb, D. J. H. Chung, and A. Riotto, "WIMPZILLAS!," Oct. 1998, *arXiv:*9810361, doi: https://doi.org/10.48550/arXiv.hep-ph/9810361

[24] S. Clesse, and J. García-Bellido, "Seven hints for primordial black hole dark matter," *Phys. Dark Univ.,* vol. 22, pp. 137-146, Dec. 2018, doi: https://doi.org/10.1016/j.dark.2018.08.004

[25] N. Sabti, J. Alvey, M. Escudero, M. Fairbairn, and D. Blas, "Refined bounds on MeV-scale thermal dark sectors from BBN and the CMB," *J. Cosmol. Astropart. Phys.,* vol. 2020, Jan. 2020, doi: https://doi.org/10.1088/1475-7516/2020/01/004

[26] K. Griest, and M. Kamionkowski, "Unitarity limits on the mass and radius of dark-matter particles," *Phys. Rev. Lett.,* vol. 64, no. 6, pp. 615-618, Feb. 1990, doi: https://doi.org/10.1103/PhysRevLett.64.615

[27] G. Arcadi et al., "The waning of the WIMP? A review of models, searches, and constraints," *Eur. Phys. J.,* vol. 78, Mar. 2018, Art. no. 203, doi: https://doi.org/10.1140/epjc/s10052-018-5662-y

[28] T. Åkesson et al., "Current Status and Future Prospects for the Light Dark Matter eXperiment," Aug. 2023, *arXiv:*2203.08192v2, doi: https://doi.org/10.48550/arXiv.2203.08192

[29] C. Ahdida et al. (The SHiP Collaboration), "Sensitivity of the SHiP experiment to light dark matter," *J. High Energy Phys.,* vol. 2021, Apr. 2021, Art. no. 199, doi: https://doi.org/10.1007/JHEP04(2021)199

[30] J. Miralda-Escude, "The Dark Age of the Universe," *Science*, vol. 300, no. 5627, pp. 1904-1909, Jun. 2003, doi: https://doi.org/10.1126/science.1085325

[31] R. Diamanti, L. Lopez-Honorez, O. Mena, S. Palomares-Ruiz, and A. C. Vincent, "Constraining dark matter late-time energy injection: decays and p-wave annihilations," *J. Cosmol. Astropart. Phys.,* vol. 2014, Feb. 2014, doi: https://doi.org/10.1088/1475-7516/2014/02/017

[32] T. R. Slatyer, "Indirect dark matter signatures in the cosmic dark ages. I. Generalizing the bound on s-wave dark matter annihilation from Planck results," *Phys. Rev. D.,* vol. 93, no. 2, p. 023527, Jan. 2016, doi: https://doi.org/10.1103/PhysRevD.93.023527

[33] P. Ciafaloni, M. Cirelli, D. Comelli, A. De Simone, A. Riotto, and A. Urbano, "On the importance of electroweak corrections for Majorana dark matter indirect detection," *J. Cosmol. Astropart. Phys.,* vol. 2011, June 2011, doi: https://doi.org/10.1088/1475-7516/2011/06/018

[34] P. Gondolo, and G. Gelmini, "Cosmic abundances of stable particles: Improved analysis," *Nucl. Phys. B,* vol. 360, no. 1, pp. 145-179, Aug. 1991, doi: https://doi.org/10.1016/0550-3213(91)90438-4

[35] S. Balan, et al., "Resonant or asymmetric: The status of sub-GeV dark matter,"*J. Cosmol. Astropart. Phys.,* vol. 2025, Jan. 2025, doi: https://doi.org/10.1088/1475-7516/2025/01/053

[36] M. Fabbrichesi, E. Gabrielli, and G. Lanfranchi, *The Physics of the Dark Photon: A Primer,* ser. SpringerBriefs in Physics, Cham, Switzerland: Springer, 2021, doi: https://doi.org/10.1007/978-3-030-62519-1

[37] P. deNiverville, C.-Y. Chen, M. Pospelov, and A. Ritz, "Light dark matter in neutrino beams: Production modeling and scattering signatures at MiniBooNE, T2K, and SHiP," *Phys. Rev. D,* vol. 95, no. 3, p. 035006, Feb. 2017, doi: https://doi.org/10.1103/PhysRevD.95.035006

[38] A. Berlin, N. Blinov, G. Krnjaic, P. Schuster, and N. Toro, "Dark matter, millicharges, axion and scalar particles, gauge bosons, and other new physics with LDMX," *Phys. Rev. D,* vol. 99, no. 7, p. 075001, Apr. 2019, doi: https://doi.org/10.1103/PhysRevD.99.075001

[39] S. Eidelman, and F. Jegerlehner, "Hadronic contributions to $(g-2)$ of the leptons and to the effective fine structure constant $\alpha(M_Z^2)$," *Z. Phys. C,* vol. 67, pp. 585-601, Dec. 1995, doi: https://doi.org/10.1007/BF01553984

[40] E. Izaguirre, G. Krnjaic, P. Schuster, and N. Toro, "Analyzing the Discovery Potential for Light Dark Matter," *Phys. Rev. Lett.,* vol. 115, no. 25, p. 251301, Dec. 2015, doi: https://doi.org/10.1103/PhysRevLett.115.251301

[41] C. Chang, P. Scott, T. E. Gonzalo, F. Kahlhoefer, A. Kvellestad, and M. White, "Global fits of simplified models for dark matter with GAMBIT," *Eur. Phys. J. C,* vol. 83, Mar. 2023, Art. no. 249, doi: https://doi.org/10.1140/epjc/s10052-023-11399-w

[42] F. Kahlhoefer, K. Schmidt-Hoberg, T. Schwetz, and S. Vogl, "Implications of unitarity and gauge invariance for simplified dark matter models," *J. High Energ. Phys.,* vol. 2016, Feb. 2016, Art. no. 16, doi:

[43] M. Dutra, M. Lindner, S. Profumo, F. S. Queiroz, W. Rodejohann, and C. Siqueira, "MeV dark matter complementarity and the dark photon portal," *J. Cosmol. Astropart. Phys.,* vol. 2018, Mar. 2018, doi: https://doi.org/10.1088/1475-7516/2018/03/037

[44] B. Batell, J. L. Feng, and S. Trojanowski, "Detecting dark matter with far-forward emulsion and liquid argon detectors at the LHC," *Phys. Rev. D,* vol. 103, no. 7, p. 075023, Apr. 2021, doi: https://doi.org/10.1103/PhysRevD.103.075023

[45] L. Bergström, T. Bringmann, and J. Edsjö, "Complementarity of direct dark matter detection and indirect detection through gamma rays," *Phys. Rev. D,* vol. 83, no. 4, p. 045024, Feb. 2011, doi: https://doi.org/10.1103/PhysRevD.83.045024

[46] R. Catena, T. Gray, and A. Lund, "On the dark matter origin of an LDMX signal," Nov. 2024, *arXiv:*2411.10216, doi: https://doi.org/10.48550/arXiv.2411.10216

[47] J. Carr, G. Lamanna, and J. Lavalle, "Indirect detection of dark matter," *Rep. Prog. Phys.,* vol. 69, no. 8, p. 2475, doi: https://doi.org/10.1088/0034-4885/69/8/R05

[48] T. Marrodán Undagoitia, and L. Rauch, "Dark matter direct-detection experiments," *J. Phys. G: Nucl. Part. Phys.,* vol. 43, no. 1, p. 013001, Dec. 2015, doi: https://doi.org/10.1088/0954-3899/43/1/013001

[49] A. Berlin, N. Blinov, S. Gori, P. Schuster, and N. Toro, "Cosmology and accelerator tests of strongly interacting dark matter," *Phys. Rev. D,* vol. 97, no. 5, p. 055033, Mar. 2018, doi: https://doi.org/10.1103/PhysRevD.97.055033

[50] J.D. Bjorken et al., "Search for neutral metastable penetrating particles produced in the SLAC beam dump," *Phys. Rev. D,* vol. 38, no. 11, pp. 3375-3386, Dec. 1988, doi: https://doi.org/10.1103/PhysRevD.38.3375

[51] B. Batell, R. Essig, and Z. Surujon, "Strong Constraints on Sub-GeV Dark Sectors from SLAC Beam Dump E137," *Phys. Rev. Lett.,* vol. 113, no. 17, p. 171802, Oct. 2014, doi: https://doi.org/10.1103/PhysRevLett.113.171802

[52] B. Aubert et al. (The BABAR Collaboration), "The BABAR Detector," *Nucl. Instrum. Methods Phys. Res. A,* vol. 479, no. 1, pp. 1-116, Feb. 2002, doi: https://doi.org/10.1016/S0168-9002(01)02012-5

[53] J.P. Lees et al. (The BABAR Collaboration), "Search for a Dark Photon in e^+e^- Collisions at BaBar," *Phys. Rev. Lett.,* vol. 113, no. 20, p. 201801, Nov. 2014, doi: https://doi.org/10.1103/PhysRevLett.113.201801

[54] A.A. Aguilar-Arevalo et al. (The MiniBooNE-DM Collaboration), "Dark Matter Search in a Proton Beam Dump with MiniBooNE," *Phys. Rev. Lett.,* vol. 118, no. 22, p. 221803, May 2017, doi: https://doi.org/10.1103/PhysRevLett.118.221803

[55] A. A. Aguilar-Arevalo et al. (The MiniBooNE Collaboration), "Low Mass WIMP Searches with a Neutrino Experiment: A Proposal for Further MiniBooNE Running," Nov. 2012, *arXiv:*1211.2258v1, doi: https://doi.org/10.48550/arXiv.1211.2258

[56] Yu.M. Andreev et al. (The NA64 Collaboration), "Search for Light Dark Matter with NA64 at CERN," *Phys. Rev. Lett.,* vol. 131, no. 16, p. 161801, Oct. 2023, doi: https://doi.org/10.1103/PhysRevLett.131.161801

[57] E. Kou et al., "The Belle II Physics Book," *Prog. Theor. Exp. Phys.,* vol. 2019, no. 12, Dec. 2019, doi: https://doi.org/10.1093/ptep/ptz106

[58] B. Abi et al., "Deep Underground Neutrino Experiment (DUNE), Far Detector Technical Design Report, Volume I: Introduction to DUNE," *J. Instrum.,* vol. 15, no. 8, Aug. 2020, doi: http://doi.org/10.1088/1748-0221/15/08/T08008

[59] L. B. Auerbach et al. (The LSND Collaboration), "Measurement of electron-neutrino electron elastic scattering," *Phys. Rev. D,* vol. 63, no. 11, p. 112001, May 2001, doi: https://doi.org/10.1103/PhysRevD.63.112001

[60] P. deNiverville, M Pospelov, and A. Ritz, "Observing a light dark matter beam with neutrino experiments," *Phys. Rev. D,* vol. 84, no. 7, p. 075020, Oct. 2011, doi: https://doi.org/10.1103/PhysRevD.84.075020

[61] C. Ahdida et al. (The SHiP Collaboration), "The SHiP experiment at the proposed CERN SPS Beam Dump Facility," *Eur. Phys. J. C,* vol. 82, May 2022, Art. no. 486, doi: https://doi.org/10.1140/epjc/s10052-022-10346-5

[62] T. Zhou, R. Plestid, K. J. Kelly, N. Blinov, and P. J. Fox, "Long-lived vectors from electromagnetic cascades at SHiP," *J. High Energy Phys.,* vol. 2025, Feb. 2025, Art. no. 107, doi: https://doi.org/10.1007/JHEP02(2025)107

[63] A. Akmete et al. (The SHiP Collaboration), "The active muon shield in the SHiP experiment," *J. Instrum.,* vol. 12, no. 5, May 2017, doi: https://doi.org/10.1088/1748-0221/12/05/P05011

[64] SHiP Collaboration & CERN HI-ECN3 Project Team, "SHiP experiment at the SPS Beam Dump Facility," Apr. 2025, *arXiv:*2504.06692v1, doi: https://doi.org/10.48550/arXiv.2504.06692

[65] M. Ferrillo, M. Ovchynnikov, F. Resnati, and A. De Roeck, "Improving the potential of BDF@SPS to search for new physics with liquid argon time projection chambers," *J. High Energy Phys.,* vol. 2024, Feb. 2024, Art. no. 196, doi: https://doi.org/10.1007/JHEP02(2024)196

[66] M. Anelli et al. (The SHiP Collaboration), "A facility to Search for Hidden Particles (SHiP) at the CERN SPS," Apr. 2015, *arXiv:*1504.04956, doi: https://doi.org/10.48550/arXiv.1504.04956

[67] S. Alekhin et al., "A facility to search for hidden particles at the CERN SPS: the SHiP physics case," *Rep. Prog. Phys.,* vol. 79, no. 12, Oct. 2016, doi: https://doi.org/10.1088/0034-4885/79/12/124201

[68] Y. S. Liu, D. McKeen, and G. A. Miller, "Validity of the Weizsäcker-Williams approximation and the analysis of beam dump experiments: Production of a new scalar boson," *Phys. Rev. D,* vol. 95, no. 3, p. 036010, Feb. 2017, doi: https://doi.org/10.1103/PhysRevD.95.036010

[69] J. D. Bjorken, R. Essig, P. Schuster, and N. Toro, "New fixed-target experiments to search for dark gauge forces," *Phys. Rev. D,* vol. 80, no. 7, p. 075018, Oct. 2009, doi: https://doi.org/10.1103/PhysRevD.80.075018

[70] K. J. Kim, and Y. S. Tsai, "Improved Weizsäcker-Williams Method and Its Application to Lepton and W-Boson Pair Production," *Phys. Rev. D,* vol. 8, no. 9, pp. 3109-3125, Nov. 1973, doi: https://doi.org/10.1103/PhysRevD.8.3109

[71] Y. S. Tsai, "Pair production and bremsstrahlung of charged leptons," *Rev. Mod. Phys.,* vol. 46, no. 4, pp. 815-851, Oct. 1974, doi: https://doi.org/10.1103/RevModPhys.46.815

[72] J. Blümlein, and J. Brunner, "New exclusion limits on dark gauge forces from proton Bremsstrahlung in beam-dump data," *Phys. Lett. B,* vol. 731, pp. 320-326, Apr. 2014, doi: https://doi.org/10.1016/j.physletb.2014.02.029

[73] E. Kriukova, "Dark photon emission in elastic proton bremsstrahlung," *Proc. Sci.,* vol. ICPPCRubakov2023, p. 011, May 2024, doi: https://doi.org/10.22323/1.455.0011

[74] D. Gorbunov, A. Makarov, and I. Timiryasov, "Decaying light particles in the SHiP experiment: Signal rate estimates for hidden photons," *Phys. Rev. D,* vol. 91, no. 3, p. 035027, Feb. 2015, doi: https://doi.org/10.1103/PhysRevD.91.035027

[75] S. Foroughi-Abari, and A. Ritz, "Dark Sector Production via Proton Bremsstrahlung," *Phys. Rev. D,* vol. 105, no. 9, p. 095045, May 2022, doi: https://doi.org/10.1103/PhysRevD.105.095045

[76] P. Ilten, J. Thaler, M. Williams, and W. Xue, "Dark photons from charm mesons at LHCb," *Phys. Rev. D,* vol. 92, no. 11, p. 115017, Dec. 2015, doi: https://doi.org/10.1103/PhysRevD.92.115017

[77] R.L. Workman et al. (Particle Data Group), "Review of Particle Physics," *Prog. Theor. Exp. Phys.,* vol. 2022, no. 8, Aug. 2022, doi: https://doi.org/10.1093/ptep/ptac097

[78] L. Buonocore, C. Frugiuele, F. Maltoni, O. Mattelaer, and F. Tramontano, "Event generation for beam dump experiments," *J. High Energy Phys.,* vol. 2019, May 2019, Art. no. 28, doi: https://doi.org/10.1007/JHEP05(2019)028

[79] K. Asai, S. Iwamoto, M. Perelstein, Y. Sakaki, and D. Ueda, "Sub-GeV dark matter search at ILC beam dumps," Jan. 2024, *arXiv:*2301.03816v2, doi: https://doi.org/10.48550/arXiv.2301.03816

[80] C. Bierlich et. al., "A comprehensive guide to the physics and usage of PYTHIA 8.3," Mar. 2022, *arXiv:*2203.11601, doi: https://doi.org/10.48550/arXiv.2203.11601

[81] L. Darmé et. al., "UFO 2.0: the 'Universal Feynman Output' format," *Eur. Phys. J. C,* vol. 83, Jul. 2023, Art. no. 631, doi: https://doi.org/10.1140/epjc/s10052-023-11780-9

[82] N. D. Christensen, and C. Duhr, "FeynRules - Feynman rules made easy," *Comput. Phys. Commun.,* vol. 180, no. 9, pp. 1614-1641, Sep. 2009, doi: https://doi.org/10.1016/j.cpc.2009.02.018

[83] A. Buckley et. al., "The HepMC3 event record library for Monte Carlo event generators," *Comput. Phys. Commun.,* vol. 260, Mar. 2021, doi: https://doi.org/10.1016/j.cpc.2020.107310

[84] P. Artoisenet et. al., "Automatic spin-entangled decays of heavy resonances in Monte Carlo simulations," *J. High Energy Phys.,* vol. 2013, no. 3, Mar. 2013, Art. no. 15, doi: https://doi.org/10.1007/JHEP03%282013%29015

[85] M. Bonesini, A. Marchionni, F. Pietropaolo, and T. Tabarelli de Fatis, "On particle production for high energy neutrino beams," *Eur. Phys. J. C,* vol. 20, pp. 13-27, Apr. 2001, doi: https://doi.org/10.1007/s100520100656

[86] B. V. Martemyanov, A. Faessler, and M. I. Krivoruchenko, "Electromagnetic form factors of nucleons in the extended vector meson dominance model," *Phys. Rev. C,* vol. 82, no. 3, p. 038201, Sep. 2010, doi: https://doi.org/10.1103/PhysRevC.82.038201

[87] C. Bierlich, G. Gustafson, and L. Lönnblad, "Diffractive and non-diffractive wounded nucleons and final states in pA collisions," *J. High Energy Phys.,* vol. 2016, Oct. 2016, Art. no. 139, doi: https://doi.org/10.1007/JHEP10%282016%29139

[88] M. Berglund, and M. E. Wieser, "Isotopic compositions of the elements 2009 (IUPAC Technical Report)," *Pure Appl. Chem.,* vol. 83, no. 2, pp. 397-410, Jan. 2011, doi: http://dx.doi.org/10.1351/PAC-REP-10-06-02

[89] D. Gorbunov, and E. Kriukova, "Dark photon production via elastic proton bremsstrahlung with non-zero momentum transfer," *J. High Energy Phys.,* vol. 2024, Jan. 2024, Art. no. 58, doi: https://doi.org/10.1007/JHEP01(2024)058

[90] L. Buonocore, C. Frugiuele, and P. deNiverville, "Hunt for sub-GeV dark matter at neutrino facilities: A survey of past and present experiments," *Phys. Rev. D,* vol. 102, no. 3, p. 035006, Aug. 2020, doi: https://doi.org/10.1103/PhysRevD.102.035006

[91] E. Akhmedov, "Majorana neutrinos and other Majorana particles: Theory and experiment," Dec. 2014, *arXiv:*1412.3320, doi: https://doi.org/10.48550/arXiv.1412.3320

A

Bilinears for Majorana Fermion Dark Matter

This appendix briefly analyzes the two bilinears relevant in the case of Majorana fermion dark matter: the vector and axial-vector currents. The starting point is the following set of properties from Eqs. (11) and (12) in [91]:

$$\bar{\psi}\Gamma\psi = \bar{\psi^c}(\mathcal{C}\Gamma^T\mathcal{C}^{-1})\psi^c, \tag{A.1}$$

$$\mathcal{C}(\gamma^\mu)^T\mathcal{C}^{-1} = -\gamma^\mu, \tag{A.2}$$

$$\mathcal{C}(\gamma^\mu\gamma^5)^T\mathcal{C}^{-1} = +\gamma^\mu\gamma^5, \tag{A.3}$$

where Γ is an arbitrary 4×4 matrix, and $\mathcal{C}$ is the charge conjugation operator, switching particles with antiparticles:

$$\hat{C} : \psi \to \psi^c \equiv \mathcal{C}\bar{\psi}^T. \tag{A.4}$$

Applying these properties to the relevant bilinears for the vector and axial-vector currents gives:

$$\bar{\psi}\gamma^\mu\psi \overset{A.1}{=} \bar{\psi^c}(\mathcal{C}(\gamma^\mu)^T\mathcal{C}^{-1})\psi^c \overset{A.2}{=} -\bar{\psi^c}\gamma^\mu\psi^c, \tag{A.5}$$

$$\bar{\psi}\gamma^\mu\gamma^5\psi \overset{A.1}{=} \bar{\psi^c}(\mathcal{C}(\gamma^\mu\gamma^5)^T\mathcal{C}^{-1})\psi^c \overset{A.3}{=} +\bar{\psi^c}\gamma^\mu\gamma^5\psi^c. \tag{A.6}$$

Using the Majorana condition $\psi^c = \psi$, the expressions simplify to:

$$\bar{\psi}\gamma^\mu\psi = -\bar{\psi}\gamma^\mu\psi, \tag{A.7}$$

$$\bar{\psi}\gamma^\mu\gamma^5\psi = \bar{\psi}(\mathcal{C}(\gamma^\mu\gamma^5)^T\mathcal{C}^{-1})\psi^c = +\bar{\psi^c}\gamma^\mu\gamma^5\psi. \tag{A.8}$$

The first identity implies that the bilinear $\bar{\psi}\gamma^\mu\psi$ identically vanishes as it is equal to its own negative. In contrast, the axial-vector term $\bar{\psi}\gamma^\mu\gamma^5\psi$ suffers no such condition, and can therefore be non-zero.

B

Differential Cross Section for π^0 Production in BdNMC

The formula in Eq. 3.18 can be obtained through:

$$\frac{d^2\sigma}{d|\vec{p}|d\theta} = \int \frac{d^3\sigma}{dp^3}\frac{dp^3}{d|\vec{p}|d\theta} = \int_0^{2\pi} \frac{d^3\sigma}{dp^3}\frac{|\vec{p}|^2\sin(\theta)d|\vec{p}|d\theta d\varphi}{d|\vec{p}|d\theta} = \tag{B.1}$$

$$= \int_0^{2\pi} d\varphi|\vec{p}|^2\sin(\theta)\frac{d^3\sigma}{dp^3} = 2\pi|\vec{p}|^2\sin(\theta)\frac{d^3\sigma}{dp^3} =$$
$$= \frac{2\pi|\vec{p}|^2\sin(\theta)}{E}(E\frac{d^3\sigma}{dp^3}) =$$
$$= \frac{2\pi|\vec{p}|^2\sin(\theta)}{\sqrt{|\vec{p}|^2+m^2}}(E\frac{d^3\sigma}{dp^3}).$$

Which is implemented in **BdNMC** through:

$$(E\frac{d^3\sigma^{pA_{target}}}{dp^3})_{\pi^0} = \left(\frac{A_{target}}{A_{Be}}\right)^{\alpha(x_F)} \cdot (E\frac{d^3\sigma^{pA_{Be}}}{dp^3})_{\pi^0} = \tag{B.2}$$

$$= \left(\frac{A_{target}}{A_{Be}}\right)^{\alpha(x_F)} \cdot \frac{1}{2}(E\frac{d^3\sigma^{pA_{Be}}}{dp^3})_{\pi^+}\left(1+\frac{1}{r_\pi}\right), \tag{B.3}$$

with functions and variables as defined in Section 3.1.2.

C

Simulation Input Card Examples

```
# Parameter card
# Mass in GeV, lengths in meters, time in seconds

# Meta Parameters
output_file ...
summary_file ...
output_mode comprehensive

burn_max 10000
burn_timeout 100000
max_trials -1
samplesize 100000
dm_energy_resolution 0.1

# Experiment Setup
beam_energy 400.0
efficiency 1 #Detector efficiency
pi0_per_POT 6
min_scatter_angle 0
max_scatter_angle 6.5973445725385655 # 2.1*pi
max_scatter_energy 1000000000.0
min_scatter_energy 0
POT 2e20
p_num_target 42 #Molybdenum 96
n_num_target 54
signal_channel NCE_electron
target_length 1.2

# Model Parameters
alpha_D 0.1
dark_matter_mass 0.001
dark_photon_mass 0.003
epsilon 0.001

# Production Channels
production_channel pi0_decay
production_distribution bmpt

production_channel eta_decay
```

```
production_distribution bmpt
meson_per_pi0 0.13333333333333333 # 0.8 (eta / POT) * 1/6 (POT / pi0)

production_channel V_decay
production_distribution proton_brem
zmin 0.1
zmax 0.9
ptmax 4

# Detector Parameters
detector cuboid
x-position 0.0
y-position 0.0
z-position 38.0
width 0.9
height 0.75
length 3.21
det-theta 0
det-phi 0
det-psi 0

# Material Parameters
material Lead
number_density 1.4548e22
proton_number 82
neutron_number 125
electron_number 82
mass 193.005578
```

Listing C.1: Example BdNMC input card.

```
# Lengths in cm and masses in GeV
import model DM_mesons_2
define darkmatter xc
define bremsstrahlung y1
decay y1 > xc xc~
generate interaction @electron
output ...
set nb_core 20
launch
set nevts_interaction 10000
set interpolation_method hist
set Z_average 82.
set A_average 207.
set prod_xsec_in_norm false
set d_target_detector 3800.00
set detector_density 5.
set off_axis False
set yc 48.9
set radius 23.
```

```
# set cylinder True
# set theta_max 0.00609749
set parallelepiped True
set x_side 90.3
set y_side 74.9
set depth 321
set ncores 8
set testplot True
set gvxd 0.
set gvxc 2.242 # This vertex has the form gvxc/2 ... in the UFO file, ->
    alpha_D = (gvxc/2)^2/4pi
set gvd11 -0.000100954
set gvu11 0.000201908
set gvd22 -0.000100954
set gvu22 0.000201908
set gvd33 -0.000100954
set gvu33 0.000201908
set gvl11 -0.000302862
set gvl22 -0.000302862
set gvl33 -0.000302862
set my1 scan1:[0.014999999999999996, 0.016113365525013256,
    0.01730936990284572, 0.018594146950147748, 0.019974285762236078,
    0.021456864505865203, 0.023049486720245937, 0.024760320312484124,
    0.02659813944743115, 0.028572369546782158, 0.03069313562820389,
    0.03297131423240377, 0.035418589204452934, 0.038047511615442585,
    0.04087156413178761, 0.043905230162300996, 0.047164068137666194,
    0.050664791303256455, 0.05442535343452561, 0.058465040914569805,
    0.06280457164608792, 0.0674662013050199, 0.07247383748079415,
    0.07785316228856283, 0.08363176408225267, 0.08983927894393418,
    0.09650754267514924, 0.10367075406969972, 0.11136565030525515,
    0.11963169535329206, 0.12851128237364168, 0.13804995113164545,
    0.14829662155296142, 0.15930384461382846, 0.17112807185350218,
    0.18382994489108095, 0.19747460643153533, 0.21213203435596423,
    0.22787740060948816, 0.24479145672737082, 0.2629609479765728,
    0.28247905823670094, 0.30344588790196453, 0.32596896725510355,
    0.3501638079461708, 0.37615449540447954, 0.4040743252219533,
    0.43406648677162796, 0.4662847975673047, 0.5008944921305863]
set mxc scan1:[0.004999999999999999, 0.0053711218416710865,
    0.0057697899676152405, 0.006198048983382587, 0.0066580952540786975,
    0.007152288168621739 5, 0.007683162240081984, 0.008253440104161371,
    0.008866046482477047, 0.009524123182260716, 0.010231045209401293,
    0.010990438077467924, 0.011806196401484313, 0.012682503871814195,
    0.01362385471059587, 0.014635076720767, 0.01572135604588874,
    0.01688826376775216, 0.01814178447817521, 0.01948834697152327,
    0.020934857215362646, 0.022488733768339958, 0.024157945826931374,
    0.0259510540961876, 0.027877254694084228, 0.02994642631464473,
    0.032169180891716415, 0.03455691802323324, 0.03712188343508507,
    0.0398772317844307, 0.04283709412454725, 0.046016650377215154,
    0.049432207184320474, 0.05310128153794282, 0.05704269061783407,
```

```
    0.06127664829702699, 0.06582486881051178, 0.07071067811865475,
    0.07595913353649607, 0.08159715224245695, 0.08765364932552429,
    0.09415968607890032, 0.10114862930065485, 0.10865632241836787,
    0.11672126931539029, 0.1253848318014932, 0.13469144174065112,
    0.144688828923876, 0.15542826585576824, 0.16696483071019547]
set wy1 auto
# bremsstrahlung paramaters
set npot 2e20
set pbeam 400. # beam energy
set ngen 100k # number of bremsstrahlung events to be generated for the
    fit
set z_min 0.1
set z_max 0.9
set pt2_max 16.
# paramaters of the fit
set nfit 100k
set nexit 1k
```

Listing C.2: Example MadDump bremsstrahlung input card.

```
# Lengths in cm and masses in GeV
import model DM_mesons_2
import_events decay ....hepmc
decay pi0 > y1 a, y1 > xc xc~
define darkmatter xc
add process interaction @electron
output ...
set nb_core 20
launch
set flux_norm 2e20 # In meson decay, set to POT
set nevts_interaction 10000
set interpolation_method hist
set Z_average 82.
set A_average 207.
set prod_xsec_in_norm false
set d_target_detector 3800.00
set detector_density 5.
set off_axis False
set parallelepiped True
set x_side 90.3
set y_side 74.9
set depth 321
set ncores 8
set testplot True
set gvxd 0.
set gvxc 2.242 # This vertex has the form gvxc/2 ... in the UFO file, ->
    alpha_D = (gvxc/2)^2/4pi
set gvd11 -0.000100954
set gvu11 0.000201908
set gvd22 -0.000100954
```

```
set gvu22 0.000201908
set gvd33 -0.000100954
set gvu33 0.000201908
set gvl11 -0.000302862
set gvl22 -0.000302862
set gvl33 -0.000302862
set my1 scan1: [0.014999999999999996, 0.016113365525013256,
    0.01730936990284572, 0.018594146950147748, 0.019974285762236078,
    0.021456864505865203, 0.023049486720245937, 0.024760320312484124,
    0.02659813944743115, 0.028572369546782158, 0.03069313562820389,
    0.03297131423240377, 0.035418589204452934, 0.038047511615442585,
    0.04087156413178761, 0.043905230162300996, 0.047164068137666194,
    0.050664791303256455, 0.05442535343452561, 0.058465040914569805,
    0.06280457164608792, 0.0674662013050199, 0.07247383748079415,
    0.07785316228856283, 0.08363176408225267, 0.08983927894393418,
    0.09650754267514924, 0.10367075406969972, 0.11136565030525515,
    0.11963169535329206, 0.12851128237364168]
set mxc scan1:[0.004999999999999999, 0.0053711218416710865,
    0.0057697899676152405, 0.006198048983382587, 0.0066580952540786975,
    0.007152288168621739 5, 0.007683162240081984, 0.008253440104161371,
    0.008866046482477047, 0.009524123182260716, 0.010231045209401293,
    0.010990438077467924, 0.011806196401484313, 0.012682503871814195,
    0.01362385471059587, 0.014635076720767, 0.01572135604588874,
    0.01688826376775216, 0.01814178447817521, 0.01948834697152327,
    0.020934857215362646, 0.022488733768339958, 0.024157945826931374,
    0.0259510540961876, 0.027877254694084228, 0.02994642631464473,
    0.032169180891716415, 0.03455691802323324, 0.03712188343508507,
    0.0398772317844307, 0.04283709412454725]
set wy1 auto

# paramaters of the fit
set nfit 100k
set nexit 1k
```

Listing C.3: Example MadDump π^0 decay input card.

D

Pythia Script

```
#include "Pythia8/Pythia.h"
#include "Pythia8Plugins/HepMC2.h"

// Pythia script for generating a HepMC file of pi0 and eta mesons from a
    proton beam hitting the molybdenum target in the SHiP experiment (To
    be used as input for maddump). Adapted to save only pi0 and eta mesons
    .


using namespace Pythia8;

int main() {

    Pythia pythia;

    // We want to do fixed target, proton on Molybdenum. Since 96Mo is not
    // a standard particle in Pythia, we add it to the database before
    // setting the beam.
    // Entries in "addParticle": id: 100ZZZAAA0, name, spintype: 2s+1,
        chargetype: (3*charge convention in order to have integers),
        colortype: 0 is uncolored, nominal mass m_0 in GeV.
    pythia.particleData.addParticle(1000420960, "96Mo", 1, 126, 0,
        89.334638710673857);

    // Interface for conversion from Pythia8::Event to HepMC event.
    // Specify file where HepMC events will be stored.
    Pythia8ToHepMC toHepMC("GAMMA.hepmc");

    pythia.readString("Beams:idA = 2212"); // Proton has PDG code 2212
    pythia.readString("Beams:idB = 1000420960"); // New Mo particle

    // Run fixed target (frametype 2). When beam energy is lower than the
        mass per nucleon, it is assumed at rest (i.e., beam B particles at
        rest here).
    pythia.readString("Beams:eA = 400");
    pythia.readString("Beams:eB = 0");
    pythia.readString("Beams:frameType = 2");

    pythia.readString("HeavyIon:SigFitNGen = 40");
```

```
    pythia.readString("SoftQCD:inelastic = on");

    // Decays //
    // When on, only particles with tau0 < tau0Max are decayed.
    pythia.readString("ParticleDecays:limitTau0 = on");
    // Default value 10 (mm/c)
    pythia.readString("ParticleDecays:tau0Max = 0");

    // The number of events to be generated.
    pythia.readString("Main:numberOfEvents = 10000");

    // If Pythia fails to initialize, exit with error.
    if (!pythia.init()) return 1;

    // Event loop
    for (int iEvent = 0; iEvent < pythia.mode("Main:numberOfEvents"); ++
        iEvent) {
        if (!pythia.next()) continue;

        // Variables to keep track of original event size and event size
            after filtering for the relevant particles (start sizeNew and
            for loop below at 3 as indices 0-2 represent: 0-system, 1 and
            2-beam particles).
        int sizeNew = 3;

        // Loop through particles in event Remove all particles except pi0
            (111) and eta (221)
        for (int i = 3; i < pythia.event.size(); ++i) {
            Particle& p = pythia.event[i];

            // Check if particle is pi0 (111) or eta (221)
            if (p.id() == 111 || p.id() == 221) {

                pythia.event[sizeNew] = pythia.event[i];
                // Particles should have mothers, so select beam particles.
                pythia.event[sizeNew].mothers(1,2);
                // Make sure particle has no daughters
                pythia.event[sizeNew].daughters(0,0);
                ++sizeNew;

                }
            }

            // Remove the sizeOld - sizeNew last particles from the event (
                i.e., the ones that did not pass the checks)
            pythia.event.popBack( pythia.event.size() - sizeNew);
            // Beam particles should have all other remaining particles as
                daughters.
            pythia.event[1].daughters( 3, sizeNew - 1);
```

```
            pythia.event[2].daughters( 3, sizeNew - 1);

        // List first compressed event.
        if (iEvent == 0) pythia.event.list();

        // Convert and write the modified event to HepMC
        toHepMC.writeNextEvent(pythia);
        }

    // Print statistics
    pythia.stat();

    // Done.
    return 0;
}
```

Listing D.1: Pythia script for generating the relevant **HepMC** file.

DEPARTMENT PHYSICS
CHALMERS UNIVERSITY OF TECHNOLOGY
Gothenburg, Sweden
www.chalmers.se

CHALMERS
UNIVERSITY OF TECHNOLOGY